Article

Developmental Cell

Chromosome Mis-segregation Generates Cell-Cycle-Arrested Cells with Complex Karyotypes that Are Eliminated by the Immune System

Graphical Abstract

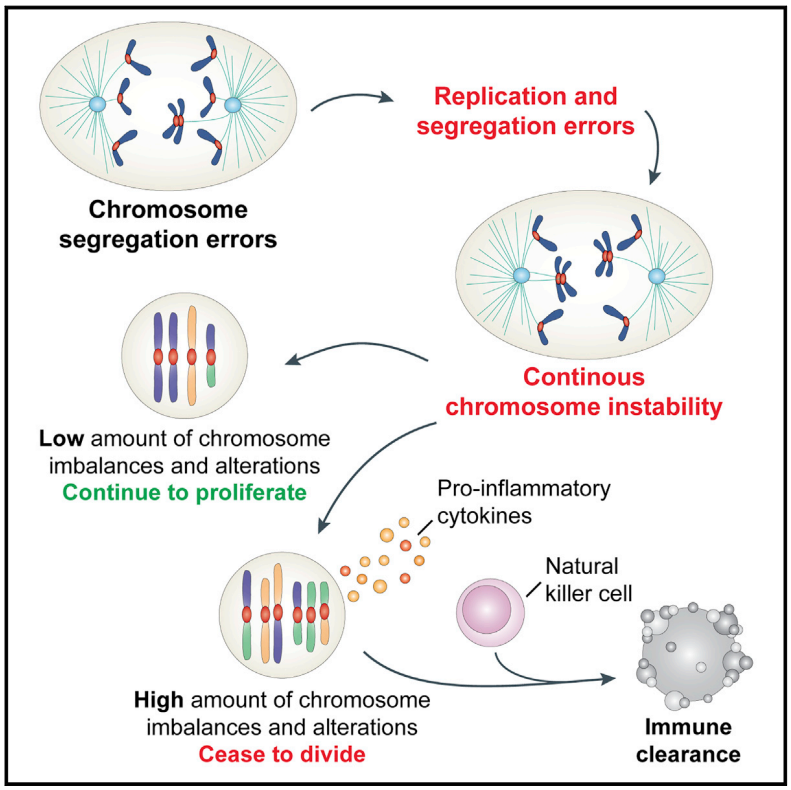

Highlights

- p53 activation is a potential, but not obligatory, outcome of chromosome mis-segregation
- Chromosome segregation errors lead to replication stress and DNA damage
- Aneuploidy drives genome instability and evolution of complex karyotypes
- Aneuploid cells with complex karyotypes are cleared by natural killer cells

Authors

Stefano Santaguida, Amelia Richardson, Divya Ramalingam Iyer, ..., Nicholas Rhind, Arshad Desai, Angelika Amon

Correspondence

ste@mit.edu (S.S.), angelika@mit.edu (A.A.)

In Brief

By examining the immediate consequences of chromosome mis-segregation, Santaguida et al. show that aneuploidy causes genomic instability and the evolution of cells with complex karyotypes. Such cells undergo senescence and produce pro-inflammatory cytokines that promote their clearance by natural killer cells.

Santaguida et al., 2017, Developmental Cell *41*, 638–651
June 19, 2017
http://dx.doi.org/10.1016/j.devcel.2017.05.022

CellPress

CellPress

Developmental Cell
Article

Chromosome Mis-segregation Generates Cell-Cycle-Arrested Cells with Complex Karyotypes that Are Eliminated by the Immune System

Stefano Santaguida,[1,*] Amelia Richardson,[2] Divya Ramalingam Iyer,[3] Ons M'Saad,[1] Lauren Zasadil,[1] Kristin A. Knouse,[1,4] Yao Liang Wong,[2,5] Nicholas Rhind,[3] Arshad Desai,[2] and Angelika Amon[1,6,*]

[1]Department of Biology, Koch Institute for Integrative Cancer Research at MIT, Howard Hughes Medical Institute, Massachusetts Institute of Technology, 76-543, Cambridge, MA 02138, USA

[2]Department of Cellular and Molecular Medicine, Ludwig Institute for Cancer Research, University of California, San Diego, La Jolla, CA 92093, USA

[3]Department of Biochemistry and Molecular Pharmacology, University of Massachusetts Medical School, 364 Plantation Street, Worcester, MA 01605, USA

[4]Division of Health Sciences and Technology, Harvard Medical School, Boston, MA 02115, USA

[5]Present address: Calico Life Sciences LLC, South San Francisco, CA 94080, USA

[6]Lead Contact

*Correspondence: ste@mit.edu (S.S.), angelika@mit.edu (A.A.)

http://dx.doi.org/10.1016/j.devcel.2017.05.022

SUMMARY

Aneuploidy, a state of karyotype imbalance, is a hallmark of cancer. Changes in chromosome copy number have been proposed to drive disease by modulating the dosage of cancer driver genes and by promoting cancer genome evolution. Given the potential of cells with abnormal karyotypes to become cancerous, do pathways that limit the prevalence of such cells exist? By investigating the immediate consequences of aneuploidy on cell physiology, we identified mechanisms that eliminate aneuploid cells. We find that chromosome mis-segregation leads to further genomic instability that ultimately causes cell-cycle arrest. We further show that cells with complex karyotypes exhibit features of senescence and produce pro-inflammatory signals that promote their clearance by the immune system. We propose that cells with abnormal karyotypes generate a signal for their own elimination that may serve as a means for cancer cell immunosurveillance.

INTRODUCTION

In all organisms analyzed to date, aneuploidy, an unbalanced karyotype in which one or more chromosomes are present in excess or reduced copy number, is highly detrimental (Santaguida and Amon, 2015a). Aneuploid budding and fission yeast show proliferation defects under standard growth conditions (Niwa et al., 2006; Torres et al., 2007). In multicellular organisms, chromosomal gain or loss is largely lethal (Hodgkin, 2005; Lindsley et al., 1972; Lorke, 1994). In humans, for example, all monosomies and most trisomies cause embryonic lethality (reviewed in Hassold and Hunt, 2001). Only trisomy of the gene poorest chromosome, chromosome 21, is compatible with survival into adulthood. However, even this trisomy leads to high levels of embryonic lethality. Only 12.5% of trisomy 21 fetuses survive to birth (reviewed in Roper and Reeves, 2006).

The adverse effects of an incorrect karyotype are also observed at the cellular level. Aneuploid mammalian and yeast cells exhibit metabolic alterations (Williams et al., 2008), proliferation defects (Santaguida et al., 2015; Stingele et al., 2012; Tang et al., 2011; Thompson and Compton, 2010; Torres et al., 2007; Williams et al., 2008), genome instability (Blank et al., 2015; Meena et al., 2015; Ohashi et al., 2015; Passerini et al., 2016; Sheltzer et al., 2011; Zhu et al., 2012), and proteotoxic stress (Oromendia et al., 2012; Santaguida et al., 2015; Santaguida and Amon, 2015b; Stingele et al., 2012; Tang and Amon, 2013), and aneuploid mammalian cells have been reported to activate p53 (Hinchcliffe et al., 2016; Li et al., 2010; López-García et al., 2017; Sansregret et al., 2017; Thompson and Compton, 2010). In addition to traits observed in a broad range of aneuploidies, aneuploid cells exhibit gene-specific phenotypes in which changes in dosage of a particular gene cause a specific phenotype (e.g., Dodgson et al., 2016).

The observation that an aneuploid karyotype has detrimental consequences on cellular fitness is consistent with the low prevalence of aneuploid cells in somatic tissues (~2%) (Knouse et al., 2014). Aneuploid cells are a rare occurrence even in tissues of mice harboring mutations that cause high levels of chromosome mis-segregation. Mice carrying a hypomorphic mutation in the spindle assembly checkpoint (SAC) component *BUB1B* (*BUB1b*$^{H/H}$ allele) exhibit high levels of chromosome mis-segregation in all tissues where this has been analyzed (Baker et al., 2004). Yet single-cell sequencing revealed aneuploid cells to be exceedingly rare in regenerating tissues such as the intestine, skin, and blood from these animals (Pfau et al., 2016). Whether aneuploid cells are outcompeted by euploid cells or whether mechanisms exist that eliminate aneuploid cells from tissues is not known.

Paradoxically, despite the adverse effects of an aneuploid karyotype on normal cell physiology, the condition is also a hallmark

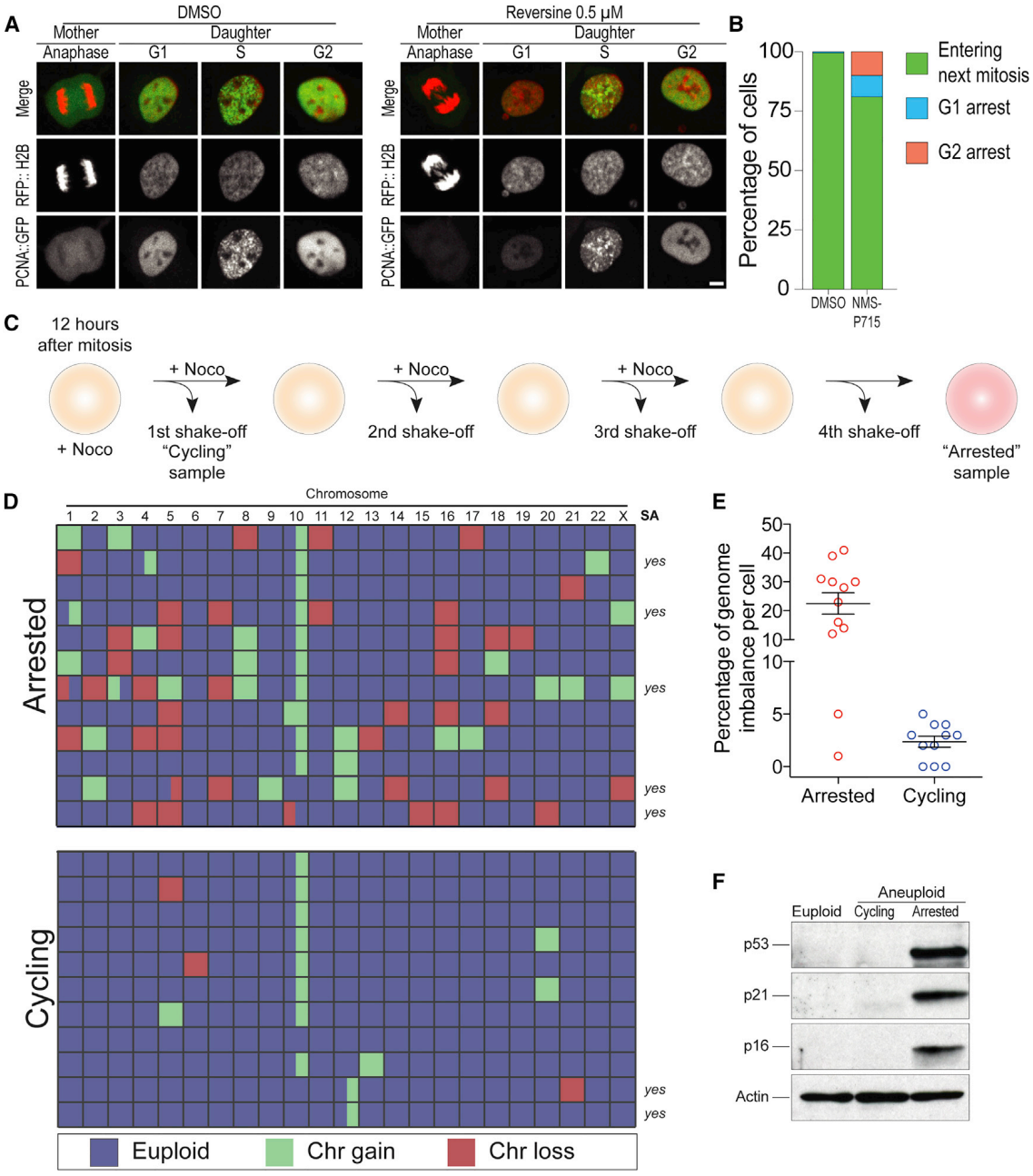

Figure 1. p53 Activation Is Not an Obligatory Consequence of Chromosome Mis-segregation

(A) Representative images of hTERT RPE1 cells co-expressing PCNA:GFP and RFP:H2B. Unsynchronized cells were treated with DMSO or 0.5 μM reversine and then immediately filmed for 48 hr. Cells were filmed every 5 min for 6 hr to capture mitotic mis-segregation events and then every 20 min for 42 hr to capture daughter cell S-phase timing. Scale bar, 5 μm.

(B) Daughter cell fate in NMS-P715-treated hTERT RPE1 cells co-expressing PCNA:GFP and RFP:H2B. Unsynchronized cells were treated with DMSO or 1 μM NMS-P715 and immediately filmed as described in (A). Bars represent percentage of daughter cells with the indicated cell fate.

(C–E) Schematic representation of experimental method used to separate cells that arrest in G_1 following chromosome mis-segregation from cells that continue to divide (C). RPE-1 cells were synchronized at the G_1/S transition by thymidine treatment. Six hours after thymidine release, cells were treated with 0.5 μM reversine for 12 hr. Six hours later, cells were treated with nocodazole. Twelve hours later, mitotic cells were removed by shake-off and single cells that detached from the plate were sequenced to determine the karyotype of cells that continue to proliferate after chromosome mis-segregation (cycling). The cells that were not removed by shake-off were placed into fresh medium containing nocodazole. This procedure was repeated three times to remove all dividing cells. The cells that remained attached to the plate represented arrested cells (arrested) and their karyotype was determined by single-cell sequencing. Heatmap in (D) shows chromosome gains and losses in the indicated cell populations. Partially colored boxes represent segmental aneuploidies and are marked as "yes" in the column SA (for segmental aneuploidies). The graph in (E) shows the degree of genome imbalance, defined as the total number of genes that are either gained or lost as a consequence of whole chromosome and segmental aneuploidies (mean ± SEM).

(legend continued on next page)

of cancer, a disease characterized by excessive cell proliferation. Ninety percent of solid tumors harbor whole chromosome gains and/or losses (Gordon et al., 2012; Holland and Cleveland, 2009). Multiple, not mutually exclusive hypotheses have been put forth to explain the prevalence of abnormal karyotypes in cancer. Chromosome copy-number alterations have been proposed to drive disease by modulating the dosage of cancer driver genes (Davoli et al., 2013). Aneuploidy also endows cells with phenotypic variability (Beach et al., 2017; Chen et al., 2015; Rutledge et al., 2016), which could help facilitate metastasis or resistance to therapeutic interventions. Indeed aneuploidy has been shown to be associated with metastatic behavior, resistance to chemotherapy and poor patient outcome (Bakhoum et al., 2011; Heilig et al., 2009; Lee et al., 2011; Walther et al., 2008). Finally, the process of chromosome mis-segregation and aneuploidy of many chromosomes have been shown to cause genomic instability (Blank et al., 2015; Crasta et al., 2012; Janssen et al., 2011; Ohashi et al., 2015; Passerini et al., 2016; Sheltzer et al., 2011; Zhu et al., 2012), which could fuel cancer genome evolution.

Given the potential link between aneuploidy and tumorigenesis, it is critical to understand how abnormal karyotypes affect cellular physiology. Here, we examine the immediate consequences of chromosome mis-segregation. We find that following chromosome mis-segregation, cells experience replication stress and genomic instability that cause the evolution of cells with highly aberrant karyotypes characterized by complex patterns of whole chromosome and segmental aneuploidies. Such cells cease to divide, undergo senescence, and produce pro-inflammatory signals that lead to their elimination by natural killer cells in vitro. Our results indicate that mechanisms exist that eliminate cells with aberrant karyotypes and thus protect organisms from cells with the potential to become cancerous.

RESULTS

Chromosome Mis-segregation Rarely Leads to p53 Activation

Previous studies reported that chromosome mis-segregation causes p53 activation and a p53-dependent cell-cycle arrest (Li et al., 2010; Thompson and Compton, 2010). The aneuploid state per se or events accompanying chromosome mis-segregation could be responsible for this p53 activation. To distinguish between these possibilities, we examined the immediate consequences of chromosome mis-segregation using live cell microscopy.

Several methods have been developed to induce chromosome mis-segregation. For example, compounds that interfere with microtubule dynamics or microtubule-kinetochore attachment cause an SAC-dependent delay in mitosis and induce chromosome mis-segregation. Inducing chromosome mis-segregation in this manner was shown to be associated with p53 activation in the subsequent G_1 phase (Thompson and Compton, 2010). However, mitotic arrest exceeding ~100 min induces a p53-dependent G_1 arrest irrespective of whether or not chromosomes are mis-segregated (Uetake and Sluder, 2010). We too observed this phenomenon. We analyzed cells that experienced an extended mitosis induced by the kinesin Eg5 inhibitor monastrol by live cell imaging (Mayer et al., 1999). This analysis showed that the frequency of chromosome mis-segregation and subsequent G_1 arrest increased with time spent in mitosis (Figure S1), highlighting that without live imaging it is difficult to compare fates of cells with and without mis-segregation due to the missing information about arrest duration.

To avoid G_1 arrest caused by a prolonged mitosis, we generated aneuploid cells by interfering with SAC function rather than by activating the checkpoint. SAC inactivation does not delay cells in mitosis but instead accelerates progression through this cell-cycle stage even when chromosomes are not attached to the spindle correctly (Figure S2A), and results in aneuploid progeny.

We examined hTERT immortalized RPE-1 cells stably expressing proliferating cell nuclear antigen (PCNA)-GFP (to determine S-phase initiation) and RFP-H2B (to monitor chromosome segregation) grown in the presence of NMS-P715 or reversine. Both compounds inhibit the SAC kinase Mps1 (Colombo et al., 2010; Santaguida et al., 2010). Treatment with NMS-P715 or reversine led to severe chromosome segregation defects. Each chromosome mis-segregated in 6%–8% of mitoses (Figures S2D–S2F and Santaguida et al., 2015) and virtually all cells harbored lagging chromosomes during anaphase and micronuclei in the following G_1 (Figures 1A, S2B, and S2C). Despite severe chromosome mis-segregation, however, mitotic arrest did not occur but cells in fact progressed through mitosis faster than vehicle-control treated cells (Figure S2A). Notably, chromosome mis-segregation did not lead to arrest in the following G_1 in the vast majority of aneuploid daughter cells (~80%; Figure 1B). This finding indicates that aneuploidy per se does not cause cell-cycle arrest in G_1.

Although 80% of cells that mis-segregated chromosomes continued to divide, 9% of cells arrested in G_1. To determine why these 9% of cells arrested in G_1, we developed a method to separate G_1-arrested cells from cycling cells following chromosome mis-segregation (Figure 1C). In brief, we induced chromosome mis-segregation and then transiently exposed cells to the microtubule poison nocodazole during the cell cycle following chromosome mis-segregation (Figure 1C). Dividing cells arrest in mitosis and can be removed from the plate by shake-off (Figure 1C). We repeated this procedure multiple times to also eliminate cells that progress through the cell cycle more slowly. The only cells that remained adhered to the plate following this procedure were cells that arrested in the interphase immediately following the mitosis during which chromosome mis-segregation was induced. Single-cell sequencing revealed highly abnormal karyotypes characterized by multiple chromosome gains and losses in cells that arrested immediately

(F) RPE-1 cells were synchronized at the G_1/S transition by thymidine treatment. Six hours after thymidine wash-out, cells were treated with 0.5 μM reversine or DMSO (vehicle control) for 12 hr. After drug wash-out, cells were grown for 66 hr (for a total of 72 hr after mitosis) to generate populations of aneuploid dividing cells (aneuploid cycling). Arrested aneuploid cells were generated as described in (C). The levels of p53, p21, and p16 were determined by western blot analysis. Actin served as a loading control.
See also Figures S1 and S2.

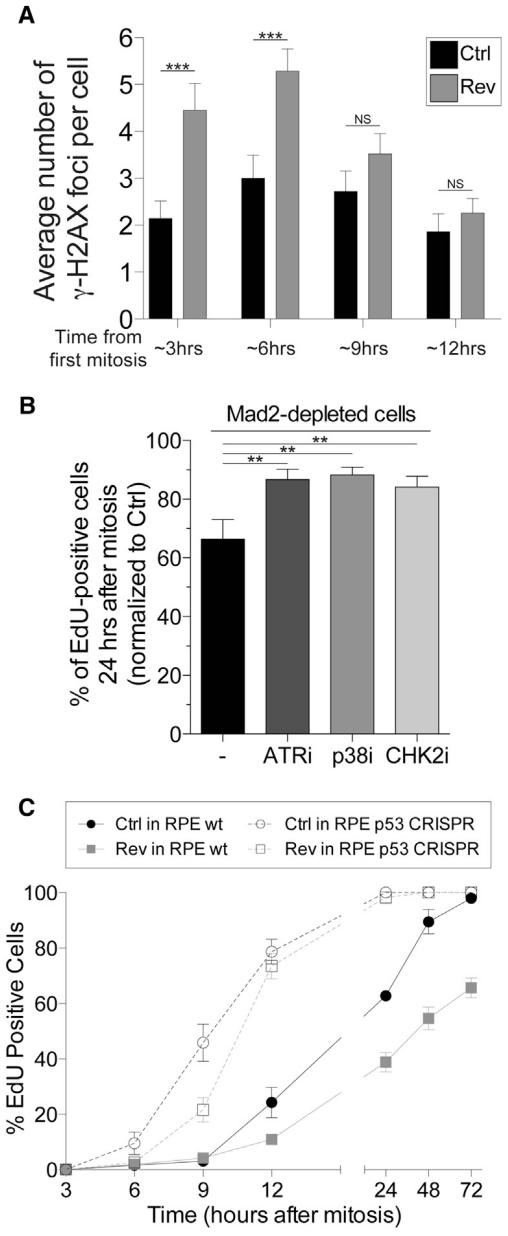

Figure 2. DNA Damage Incurred during Chromosome Mis-segregation Causes p53 Activation

(A) RPE-1 cells were synchronized at the G_1/S transition by thymidine treatment. After thymidine wash-out, cells were treated with 0.5 μM reversine or DMSO (vehicle control). The average number of γ-H2AX foci per cell was determined at the indicated times (mean ± SEM). ***$p < 0.0001$; NS, not significant (ANOVA plus Bonferroni's test). F test of variance: 3-hr time point, 7.54718×10^{-5}; 6-hr time point, 0.002922704.

(B) RPE-1 cells were exposed to a single round of small interfering RNA (siRNA)-mediated depletion of Mad2 or control (Ctrl) oligo followed by thymidine arrest. Fourteen hours after thymidine wash-out (which corresponds roughly to 2 hr after mitosis), control- and Mad2-depleted cells were exposed to the indicated kinase inhibitors and 5-ethynyl-2′-deoxyuridine (EdU). The percentage of EdU-positive cells was determined 36 hr after thymidine release (~24 hr after mitosis). The graph shows the percentage of EdU-positive cells normalized to control-depleted cells. The following small-molecule inhibitors were used: VE821 (ATR inhibitor, working concentration 1 μM), SB203580 (p38 inhibitor, working concentration 10 μM), Chk2 inhibitor II (Chk2 inhibitor, working concentration 10 μM). Graph shows mean ± SEM. **$p < 0.01$, ANOVA plus Bonferroni's test.

(C) RPE-1 cells, either wild-type for p53 or lacking the tumor suppressor (p53 CRISPR), were synchronized at the G_1/S transition by thymidine treatment. After thymidine wash-out, cells were treated with 0.5 μM reversine or DMSO (vehicle control). Fourteen hours later, the drug was washed out and cells were exposed to EdU. Percentage of EdU-positive cells was determined at the indicated times. Graph shows mean ± SEM.

See also Figure S3.

following chromosome mis-segregation (Figures 1D and 1E). Whereas aneuploid cells that still divided harbored genomic imbalances, which involved less than 5% of their genomes, aneuploid arrested cells exhibited genomic imbalances involving more than 20% of their genomes (Figure 1E). In addition to whole chromosome gains and losses, 42% of cells that had arrested in G_1 (5 out of 12 cells) also harbored segmental aneuploidies compared with about 18% of aneuploid cells that were still able to divide (2 out of 11 cells; note that the segmental gain on chromosome 10 was not included in this analysis as it is a characteristic of RPE-1 cells [Zhang et al., 2015]). Aneuploid arrested cells also exhibited signs of cellular senescence. Levels of p53, and the CDK inhibitors p21 and p16, were elevated (Figure 1F).

Inactivation of the DNA Damage Checkpoint Suppresses the G_1 Arrest Following Chromosome Mis-segregation

Segmental aneuploidies in G_1 arrested aneuploid cells could be the result of DNA damage incurred during cytokinesis (Janssen et al., 2011), during accelerated anaphase entry (Figure S2A), or in micronuclei (Crasta et al., 2012). Their presence in G_1 arrested aneuploid cells thus raised the possibility that cell-cycle arrest was due to DNA damage associated with chromosome mis-segregation. To test this we analyzed γ-H2AX levels following chromosome mis-segregation. Although not detectable by western blot analysis (Figure S3A), we observed a transient, modest increase in the average number of γ-H2AX foci 3–6 hr after chromosome mis-segregation (Figures 2A, S3B, and S3C; Janssen et al., 2011). More importantly, preventing activation of the DNA damage response by inhibiting the DNA damage response kinases ATR, p38, or CHK2 or inactivation of p53 partially suppressed the infrequent G_1 delay following chromosome mis-segregation (Figures 2B, 2C, and S3D). These findings suggest that DNA damage occurring during chromosome mis-segregation might be responsible for the G_1 arrest following chromosome mis-segregation in a small number of cells. Support for this conclusion comes from the finding that constitutive aneuploidies do not elicit a p53 response. Mouse embryonic fibroblasts (MEFs) trisomic for various different chromosomes do not activate p53 (Tang et al., 2011), nor does p53 depletion suppress their proliferation defects (Sheltzer et al., 2017). It is also possible that stresses associated with aneuploidy, such as oxidative and proteotoxic stress, which scale with the degree of aneuploidy, cause p53 activation. Indeed, we note that cells which arrest in G_1 and activate p53 following chromosome mis-segregation harbor highly aberrant karyotypes (Figure 1D).

Aneuploidy Causes DNA Replication Defects

While aneuploidy per se did not impair G_1 progression, it was possible that other cell-cycle stages were affected by an

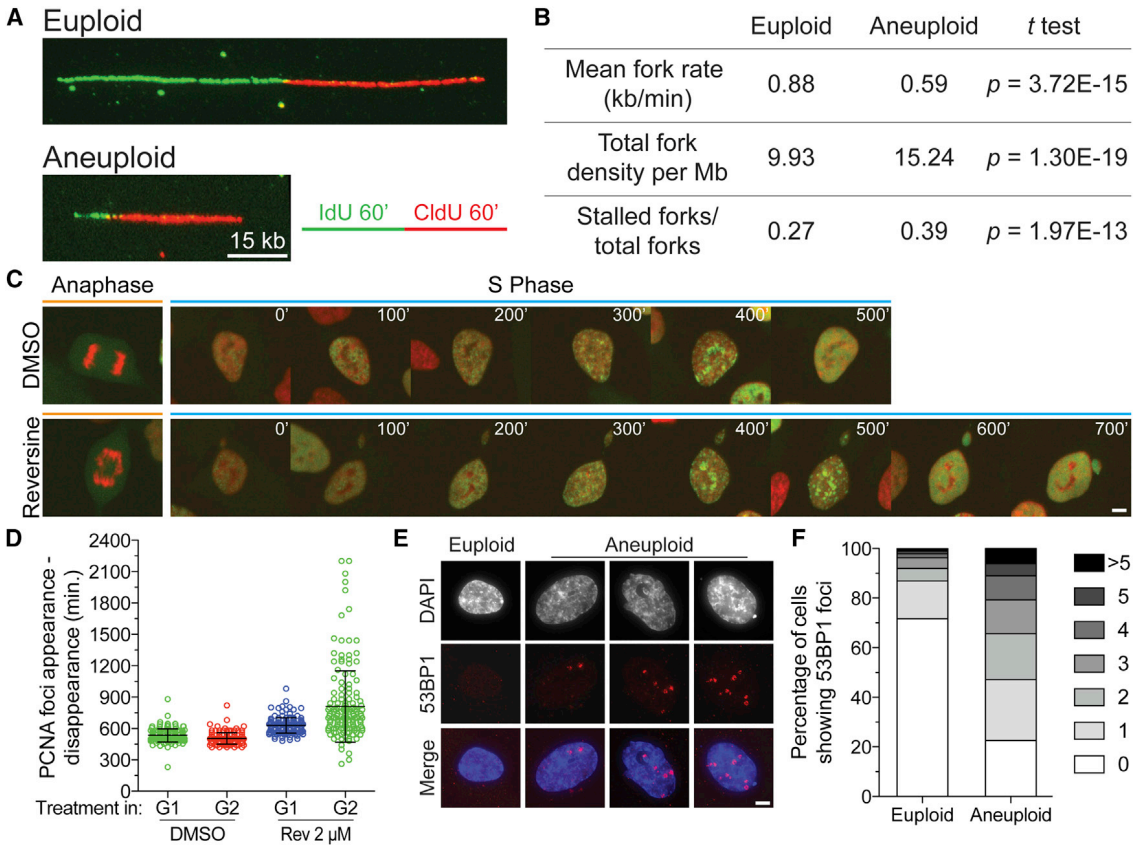

Figure 3. Chromosome Mis-segregation Causes Replication Stress

(A and B) RPE-1 cells were treated with reversine (0.5 μM; aneuploid) or vehicle control (euploid) for 24 hr. The inhibitor was then washed out and cells were arrested in G_1 by treatment with mimosine for 24 hr. After mimosine wash-out, cells were placed into fresh medium and 3 hr later pulse labeled with IdU (5-iodo-2′-deoxyuridine; green) for 60 min and chased with CldU (5-chloro-2′-deoxyuridine; red) for 60 min. Sample fiber images from euploid and aneuploid cells are shown in (A). Fork rate, fork density, and fork stall rate are shown in (B).

(C and D) Unsynchronized RPE-1 cells co-expressing PCNA:GFP and RFP:H2B were treated with DMSO or reversine (2 μM), imaged every 5 min for 5 hr to capture mitotic mis-segregation events, and imaged every 20 min for 48 hr to capture daughter cell S-phase timing. Representative images of mother cell anaphase and one daughter cell S phase after treatment with DMSO or reversine are shown in (C). Quantification of the time interval from PCNA focus appearance to dissolution, a measure for S-phase duration in living cells, is shown in (D). The analysis was performed on daughter cells whose mother cells divided prior to addition of reversine (reversine exposure occurred during G_1) and on daughter cells whose mothers mis-segregated chromosomes in the presence of reversine (reversine exposure occurred during G_2; mean ± SD). Scale bar, 5 μm.

(E and F) RPE-1 cells were treated with 0.5 μM reversine or vehicle control for 24 hr. The drug was then washed out and cells were synchronized in G_1 using mimosine for 24 hr. After mimosine wash-out, cells were placed into fresh medium and 53BP1 foci were analyzed 4 hr later. Representative images (E) and quantification (F) are shown. Scale bar, 5 μm.

See also Movie S1.

unbalanced karyotype. Previous studies in budding yeast and human cells showed that many but not all aneuploidies cause DNA replication defects and genomic instability because of changes in gene copy number of factors critical for DNA replication and segregation (Blank et al., 2015; Meena et al., 2015; Ohashi et al., 2015; Passerini et al., 2016; Sheltzer et al., 2011; Zhu et al., 2012). To assess the immediate effects of chromosome mis-segregation on the subsequent S phase, we induced chromosome mis-segregation using reversine (aneuploid) or did not interfere with mitosis (euploid), then synchronized cells in G_1 and measured DNA replication fork rate by DNA combing after release from the G_1 arrest. Fork rates were significantly slower in cells that had mis-segregated their chromosomes compared with their euploid counterparts (0.59 ± 0.02 kb min^{-1} versus 0.88 ± 0.03 kb min^{-1}; Figures 3A and 3B). Furthermore, replication fork stalling was increased in aneuploid cells (Figure 3B). Live cell imaging of reversine-treated cells confirmed this result (Figures 3C and 3D; Movie S1). PCNA foci, a sign of ongoing DNA replication, persisted for longer times in cells that had mis-segregated their chromosomes in the preceding mitosis (Figure 3D). The prolonged presence of PCNA foci in cells was not a consequence of reversine treatment. Cells that were in G_1 at the time of reversine treatment (cells that had completed mitosis but did not harbor PCNA foci at the time of reversine addition) were slightly delayed in S phase by reversine treatment (Figures 3D and Table S1; compare G_1 population ± reversine), but this delay was not nearly as dramatic as that of cells that had mis-segregated chromosomes because reversine was added prior to mitosis (Figure 3D; compare G2 population ± reversine). Not surprisingly, DNA replication defects were

accompanied by DNA damage as judged by an increase in 53BP1 foci (Figures 3E and 3F). Our results indicate that chromosome mis-segregation leads to DNA replication stress in the following S phase, which results in DNA damage. We propose that genomic imbalances caused by the aneuploid state as well as replication problems in micronuclei are causes of this replication defect (Passerini et al., 2016).

Chromosome Mis-segregation Triggers the Evolution of Complex Abnormal Karyotypes

What are the consequences of aneuploidy-induced DNA damage? Do such cells permanently arrest in G_2 or do some of them proceed to mitosis? Our immunofluorescence studies indicate that the latter occurs. We observed DNA damage to persist into pro-metaphase. Aneuploid pro-metaphase cells harbored increased levels of γ-H2AX foci compared with euploid cells but lower than those seen in cells treated with aphidicolin, which interferes with replication of late replicating regions of the genome and results in DNA damage persisting into prometaphase (Figures 4A and 4B; Minocherhomji et al., 2015).

To further characterize how chromosome mis-segregation affects genome integrity, we analyzed the cell division following the mitosis during which cells were treated with reversine by live cell microscopy (henceforth second mitosis; Figure 4C). Aneuploid cells exhibited a high degree of mitotic aberrations during the second mitosis, lagging chromosomes during anaphase and micronuclei in the following G_1 (Figures 4D, 4E, and S4; Movie S2). Importantly, these abnormalities were not due to incomplete drug wash-out and, hence, lack of an SAC function. Duration of the abnormal second mitoses was significantly longer than that of unperturbed mitoses, indicating that the spindle assembly checkpoint was active (Figure 4F). Furthermore, we observed ultrafine anaphase DNA bridges—DNA threads that connect under-replicated genomic regions—as revealed by staining with antibodies against the Bloom's syndrome helicase (BLM) protein and Plk1-interacting checkpoint helicase (PICH) protein (Figure 4G).

Signs of DNA damage, identified as 53BP1 foci, were apparent even in G_1 following this second mitosis (Figures 5A and 5B). Comparison of the karyotypes of cells immediately after chromosome mis-segregation (''First cell cycle'' in Figures 5C, 5D, and S5A) and of cells that had undergone an additional mitosis thereafter confirmed that complex karyotypes evolve in aneuploid cells (''Second cell cycle'' in Figures 5C, 5D, and S5B). Only 20% of cells displayed greater than two chromosome aberrations immediately after chromosome mis-segregation (Figures 5C and 5D, in agreement with Figures S2C–S2F and Colombo et al., 2010; Hewitt et al., 2010; Santaguida et al., 2015, 2010), but in the second mitosis, 80% of cells harbored more than two chromosome gains or losses (Figure 5). Together, our results indicate that chromosome mis-segregation has consequences beyond the production of cells with whole chromosome gains or losses. It sets in motion a process whereby replication stress and DNA damage drive chromosome segregation errors and mitotic aberrations in the next mitosis.

Cells with Complex Karyotypes Senesce

Our results indicate that chromosome mis-segregation leads to the generation of cells with highly aberrant karyotypes. Their ability to undergo mitosis decreased as karyotypes became more aberrant (Figure 6A), indicating that they arrest in interphase. To characterize the cells that had stopped proliferating within 3 days after they had been induced to mis-segregate their chromosomes, we induced chromosome mis-segregation, allowed cells to divide for 3 days, and repeatedly used the previously described nocodazole shake-off protocol to remove cells that were still proliferating, which we determined to be approximately 60% (Figure 6B). Of the 40% of cells that had arrested within 3 days following chromosome mis-segregation, approximately half had never undergone a cell division and the other half had undergone at least one cell cycle as judged by 5-ethynyl-2′-deoxyuridine (EdU) incorporation (Figure 6C).

The cell population obtained in this manner exhibited the same characteristics as cells that arrested in G_1 immediately following chromosome mis-segregation. They harbored highly abnormal karyotypes with multiple whole chromosome and segmental aneuploidies (Figures 6D and 6E) and displayed the hallmarks of senescence, including elevated levels of the senescence markers p53, p21, and p16 (Figure 6F), higher numbers of γ-H2AX foci (Figure 6G), and increased senescence-associated β-galactosidase activity (Figure 6H and Baker et al., 2004).

Like cells that arrest in G_1 immediately following chromosome mis-segregation, inactivation of p53 partially suppressed their cell-cycle arrest. We induced chromosome mis-segregation, removed proliferating cells by nocodazole shake-off, and determined the number of cells that detached from the plate as a measure of the percentage of the population that continued to proliferate following chromosome mis-segregation. This analysis revealed that fewer aneuploid cells arrested in interphase when p53 was deleted compared with aneuploid cells with intact p53 (Figure 6I). Our results indicate that approximately 50% of cells arrest in G_1 due to p53 activation whereas other pathways prevent cell proliferation in the other half of G_1 cells.

The Aneuploid State Causes a Senescence-Associated Gene Expression Signature

Gene expression analysis of the G_1 arrested aneuploid cells was consistent with cells being senescent. We observed downregulation of genes involved in cell-cycle progression (Figures S6A–S6C) and a senescence-associated gene expression profile known as senescence-associated secretory phenotype (SASP) (Freund et al., 2010) (Figure S6D and Table S2; the leading edge of the enrichment includes the genes listed in Table S3). DNA damage and cell-cycle arrest are likely a major cause of the SASP gene expression signature observed in cells with complex karyotypes, although other aspects of the aneuploid state likely also contribute. MEFs harboring specific trisomies also show an SASP gene expression pattern (Figure S6E and Sheltzer et al., 2012), yet these cells do not experience significant DNA damage nor activate p53 nor undergo cell-cycle arrest (Figure S6F) (Tang et al., 2011; Williams et al., 2008).

Cells with Complex Karyotypes Produce Pro-inflammatory Signals

Our gene expression analysis not only revealed the existence of an SASP-like gene expression signature in aneuploid cells but also the upregulation of genes that mediate inflammation and an immune response (Figure 7A). The top seven upregulated

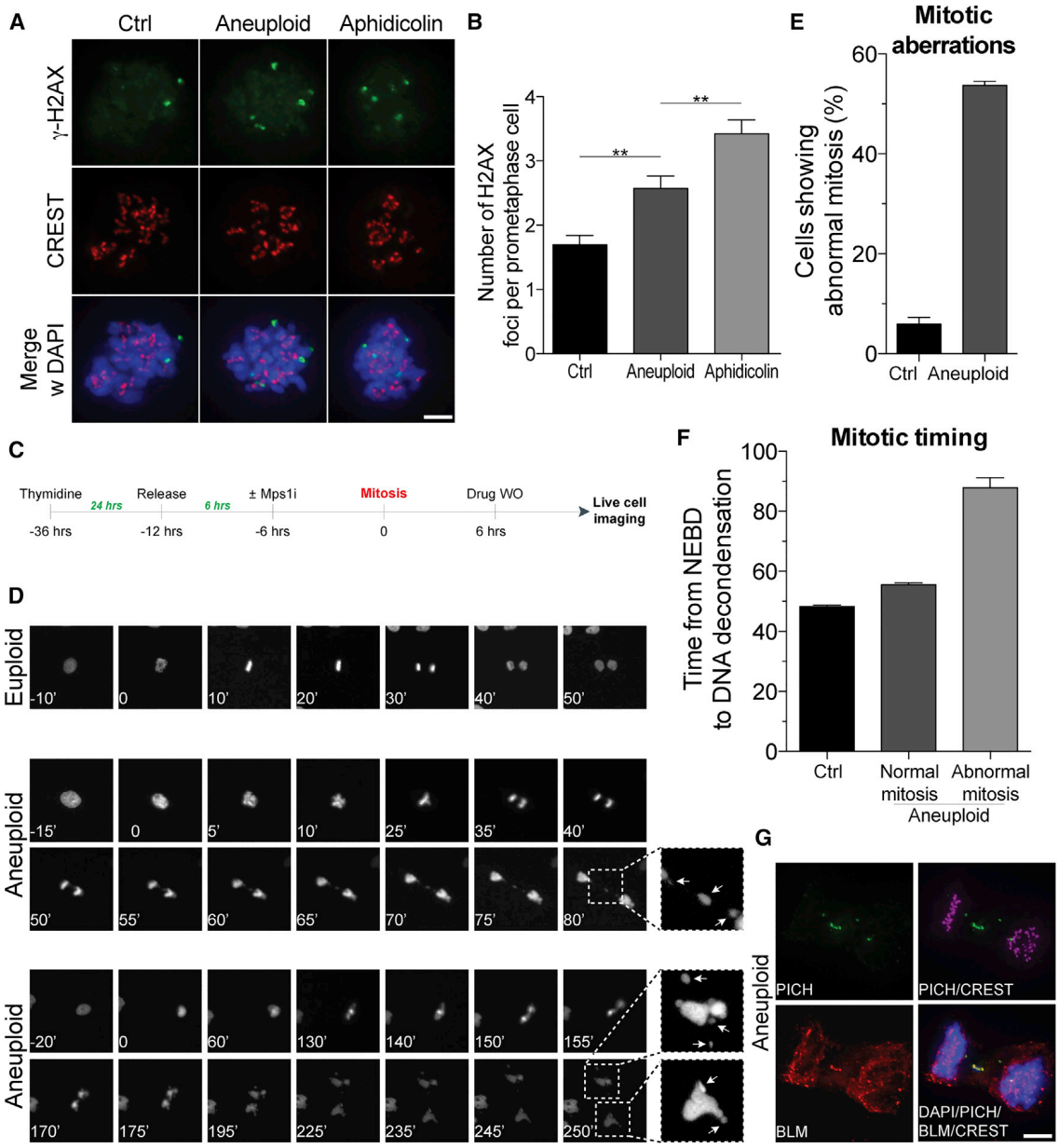

Figure 4. Chromosome Mis-segregation Results in Genomic Instability

(A and B) RPE-1 cells were synchronized at the G_1/S transition by thymidine treatment. Six hours after thymidine release, cells were treated with control vehicle (euploid) or 0.5 μM reversine (aneuploid) for 12 hr. Twelve hours after drug wash-out, cells were treated with the CDK1 inhibitor RO-3306 for 12 hr to enrich for G2 cells. Cells were then released in fresh medium containing nocodazole and γ-H2AX foci were analyzed 2 hr later. CREST was used to mark centromeres. As a positive control, cells were treated with aphidicolin 18 hr after thymidine release. Representative images are shown in (A). Quantification of γ-H2AX foci is shown in (B). γ-H2AX is in green, CREST in red, and DNA in blue (mean ± SEM). Scale bar, 10 μm. $^{**}p < 0.01$, ANOVA plus Bonferroni's test.

(C–F) RPE-1 cells stably expressing H2B-GFP were synchronized at the G_1/S transition by thymidine treatment. Six hours after thymidine wash-out, cells were treated with control vehicle (euploid) or 0.5 μM reversine (aneuploid) for 12 hr. After drug wash-out, cells were filmed every 5 min. Schematic representation of experimental method is shown in (C). Representative images from live imaging datasets are shown in (D). Arrows show lagging chromosomes and micronuclei. Quantification of mitotic aberrations (lagging chromosomes and micronuclei) is shown in (E). Length of mitosis (nuclear envelope breakdown [NEBD] to DNA decondensation) is shown in (F) (mean ± SEM).

(G) Cells were grown as described in (A). After RO-3306 wash-out, cells were released into fresh medium and fixed 90 min later to analyze DNA bridges in anaphase. Representative images of DNA bridges are shown. PICH is in green, BLM in red, CREST in magenta, and DNA in blue. Scale bar, 10 μm.

See also Figure S4 and Movie S2.

gene set categories in arrested cells with complex karyotypes represented gene expression profiles associated with an immune response. Interestingly, with the exception of the "Interferon alpha/beta signaling" gene set, immune response gene sets observed in aneuploid arrested cells did not match gene sets previously identified in cells in which senescence was

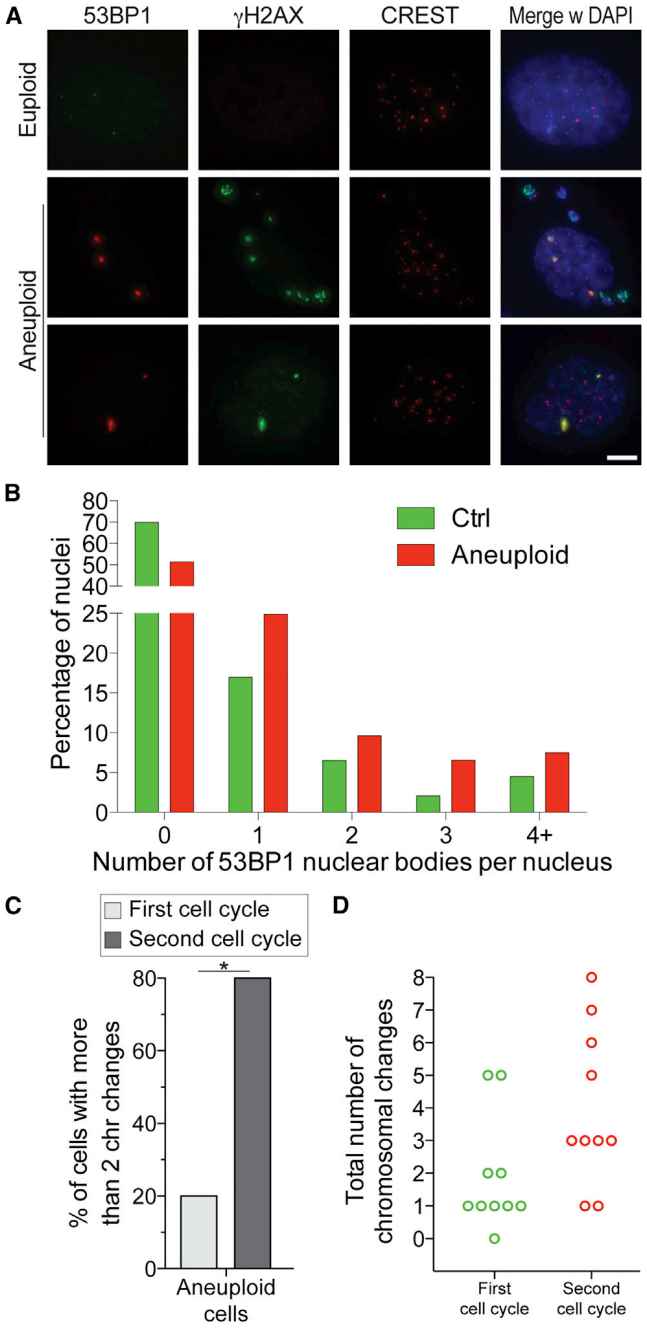

Figure 5. Chromosome Mis-segregation Triggers the Evolution of Complex Abnormal Karyotypes

(A and B) Cells were grown as described in Figure 4A. After RO-3306 wash-out, cells were released into fresh medium and fixed 6 hr later to analyze 53BP1 foci in the following G_1. Representative images are shown (A). 53BP1 is in red, γ-H2AX in green, CREST in magenta, and DNA in blue. Quantification of 53BP1 foci in G_1 is shown in (B). Scale bar, 5 μm.

(C and D) Karyotype analysis after the first and second cell cycle following chromosome mis-segregation (see Figure S5 for experimental details). The percentage of cells with more than two chromosome changes (C) and the total number of chromosomal changes per cell (D) are shown for aneuploid cells after the first and second cell cycle following chromosome mis-segregation. *$p < 0.05$, Student's t test.

See also Figure S5.

induced by DNA damage (Figure 7A and Krizhanovsky et al., 2008). Furthermore, we found the cGAS/STING pathway, an innate immune system pathway that is activated in response to cytosolic DNA, to be upregulated in cells with complex karyotypes (Schneider et al., 2014) (Figure S7G and Table S2). Whether these findings indicate that aneuploid arrested cells exhibit a different immune response than cells that senesce due to DNA damage remains to be determined. We conclude that cells that arrest in G_1 with highly abnormal karyotypes induce multiple immune response pathways. In agreement with the idea that the aneuploid state produces a pro-inflammatory signal is the recent finding that fibroblasts derived from Down syndrome individuals activate an interferon response (Sullivan et al., 2016).

Consistent with the inflammatory gene expression profile observed in cells with complex karyotypes, we found the secretion of cytokines (interleukin-6 [IL-6], IL-8, and CCL2) to be elevated (Figure 7B). Interestingly, we also observed a subtle elevation in secretion of CCL2 but not other cytokines in early-passage MEFs derived from *BUB1b*$^{H/H}$ (Figure 7C), which do not exhibit signs of senescence. This finding raises the interesting possibility that increased immunogenicity is not just a characteristic of cells with complex karyotypes that ceased to divide but also of cells with aberrant karyotypes that are proliferating.

To further characterize the immunogenic potential of arrested aneuploid cells, we examined various cell-surface proteins known to trigger recognition by the innate immune system, specifically natural killer (NK) cells. First, we examined expression of MICA and MICB. MICA and MICB are cell-surface proteins that belong to the NK group 2, member D (NKG2D) ligand family, and activate NK cells in response to proteotoxic stress (Raulet and Guerra, 2009). Although euploid cells expressed MICA and MICB at their cell surface, MICA/B levels were elevated 2-fold in arrested aneuploid cells (Figures 7D and 7G; Chien et al., 2011; Krizhanovsky et al., 2008). This increase was not due to differences in cell size between aneuploid and euploid cells, as we compared MICA/B mean fluorescence intensity between cell populations of the same size (Figure S7A). We also examined the expression of the NKG2D ligands ULBP1 and ULBP2 at the cell surface. ULBP1 and ULBP2 are induced by cellular stresses and DNA damage (Raulet and Guerra, 2009). Their levels were also elevated in aneuploid arrested cells compared with euploid cells but did not reach levels seen in euploid cells treated with the DNA-damaging agent doxorubicin (Figures 7E, 7G, and S7B–S7D).

DNAM1 is an adhesion molecule at the surface of NK cells which mediates interactions between NK cells and target cells (Raulet and Guerra, 2009). This protein binds to CD112 (also known as Nectin-2) and CD155 (also known as PVR), two surface molecules expressed in response to DNA damage (Raulet and Guerra, 2009). Aneuploid cells expressed CD112 and CD155 at elevated levels (Figures 7F, 7G, and S7E–S7G). CD155 levels, in particular, were as high in aneuploid arrested cells with complex karyotypes as in euploid cells treated with doxorubicin (Figures 7F and 7G). Finally, we found phosphorylation of STAT3 (Y705) and SAPK/JNK (T183/Y185) (Figure 7H) to be higher in aneuploid arrested cells, which suggests that the inflammatory response caused by arrested cells with complex karyotypes triggers a feedforward loop in which secreted cytokines propagate the inflammation response by activating other inflammatory

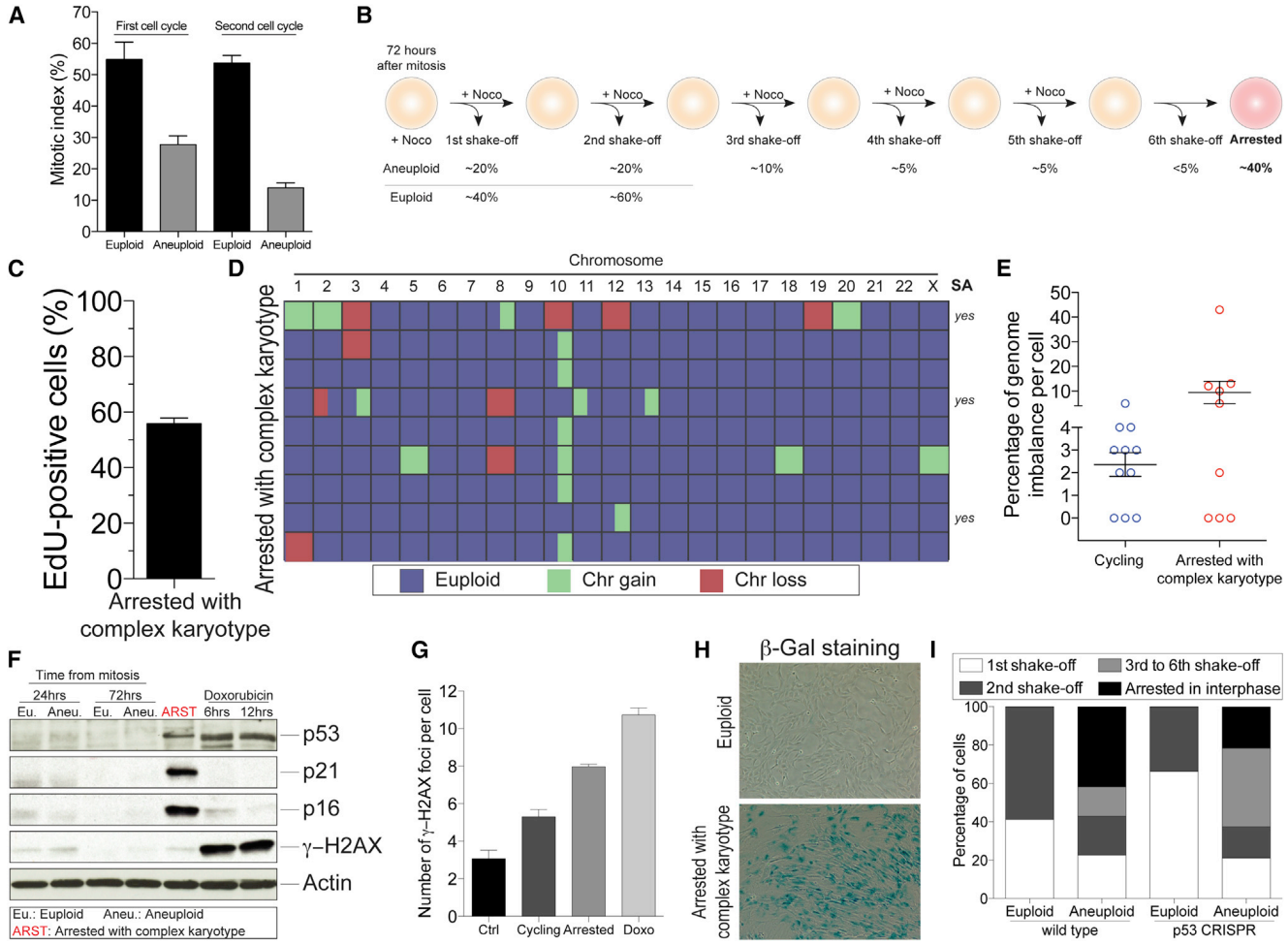

Figure 6. Chromosome Mis-segregation Causes the Generation of Cells with Complex Karyotypes that Undergo Senescence

(A) RPE-1 cells were treated with reversine or control vehicle for 24 hr. Cells were exposed for 12 hr to nocodazole either after wash-out or 24 hr later, to determine the ability of cells to enter mitosis during the first or second cell cycle following chromosome mis-segregation (mean ± SEM).

(B) Schematic representation of the experimental method used to isolate arrested cells with complex karyotypes (see STAR Methods for details). Shown below the cartoon is the percentage of cells that detached from the plate after each shake-off.

(C) Aneuploid arrested cells were isolated as described in STAR Methods. Cells were exposed to EdU after reversine wash-out, plated on coverslips after the fourth nocodazole shake-off, and fixed 12 hr later to determine the percentage of EdU-positive cells. Graph shows mean ± SEM.

(D and E) Aneuploid arrested cells were isolated as described in STAR Methods and their karyotype determined by single-cell sequencing. The heatmap of chromosome gains and losses of arrested cells with complex karyotypes is shown in (D). Partially colored boxes represent segmental aneuploidies and are marked as "yes" in the column SA (for segmental aneuploidies). The graph in (E) shows the degree of genome imbalance, defined as the total number of genes that are either gained or lost as a consequence of whole chromosome and segmental aneuploidies (mean ± SEM). The "Cycling" sample is the same as presented in Figure 1E and is composed of aneuploid cells able to divide.

(F) RPE-1 cells were synchronized at the G_1/S transition by thymidine treatment. Six hours after thymidine release, cells were treated with DMSO (euploid) or 0.5 μM reversine (aneuploid) for 12 hr. After wash-out, cells were placed into fresh medium and harvested 18 or 66 hr later, which corresponds to 24 and 72 hr after mitosis, respectively. Arrested cells were obtained as described in (B). The levels of p53, p21, p16, and γ-H2AX were determined by western blot analysis. Actin served as a loading control. Euploid cells treated with doxorubicin for 6 or 12 hr were used as positive controls. Euploid and aneuploid samples represent cells that were initially treated with DMSO or 0.5 μM reversine, respectively.

(G) Euploid, aneuploid cycling, and aneuploid arrested cells were generated as described in STAR Methods. The graph shows the quantification of γ-H2AX foci per cell. Euploid cells treated with doxorubicin for 12 hr were used as a positive control. Graph shows mean ± SEM.

(H) Senescence-associated β-galactosidase (β-Gal) activity was determined in euploid cells and arrested cells with complex karyotypes obtained as described in (B).

(I) The percentage of cycling and arrested euploid or aneuploid RPE-1 cells, either wild-type or lacking p53, was determined following the scheme shown in (B). Graph shows the percentage of arrested cells or cells recovered after the indicated mitotic shake-offs.

See also Tables S2 and S3.

pathways such as those dependent on STAT3 and SAPK/JNK (Kyriakis and Avruch, 2001). Together, these findings indicate that aneuploid arrested cells elicit an immune response.

To test whether aneuploid arrested cells were indeed targeted by immune cells, we co-cultured euploid cells or aneuploid arrested cells with NK92 cells and followed cell viability by live

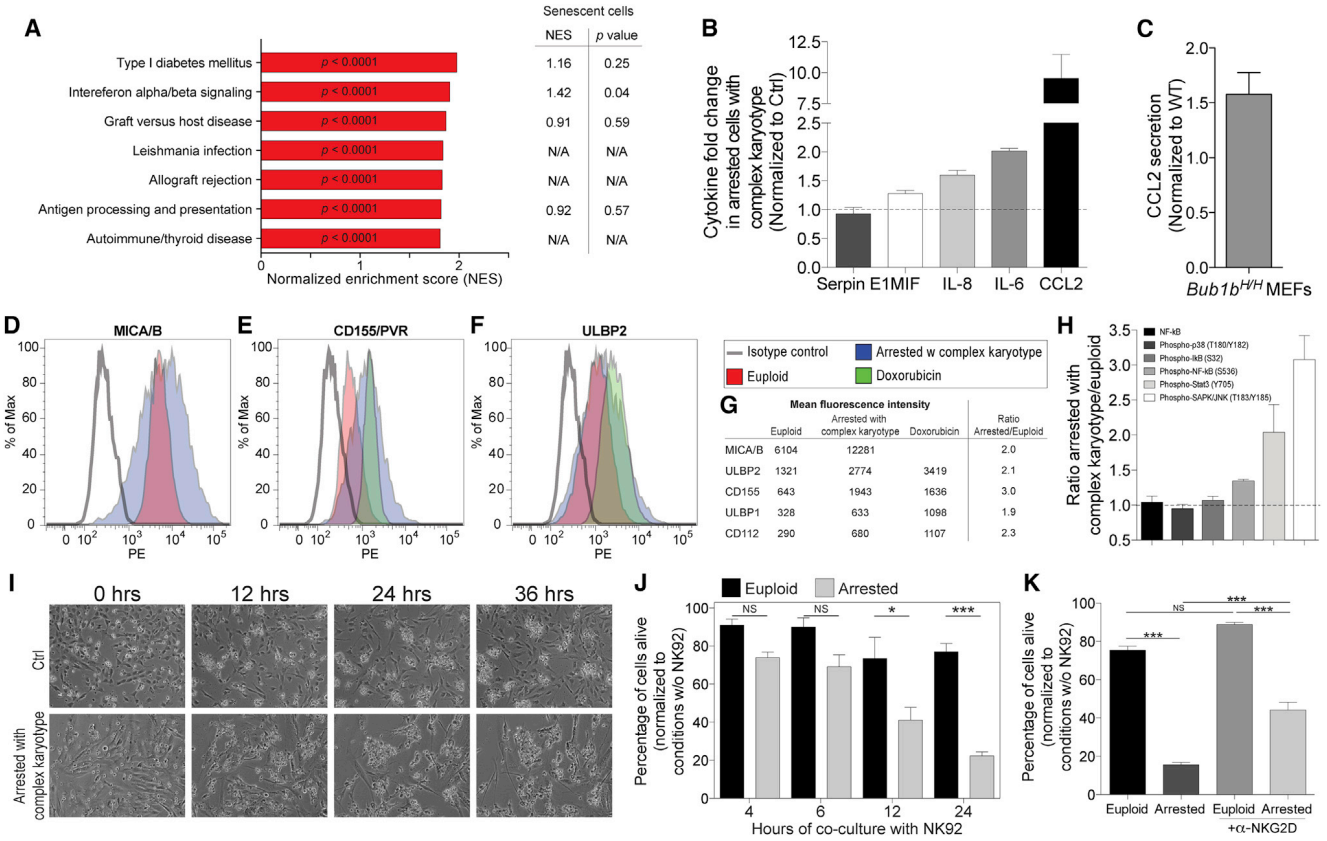

Figure 7. Aneuploidy Triggers an Immune Response

(A) Canonical pathway gene set (c2cp of msigdb) enrichment for upregulated genes in arrested cells with complex karyotypes. Normalized enrichment scores (NES) for the top seven upregulated gene sets are shown. The columns on the right show the normalized enrichment score for these gene categories in gene expression datasets obtained from cells in which senescence was induced by DNA damage (Iannello et al., 2013; Krizhanovsky et al., 2008).

(B) Cytokine levels were determined in supernatants of euploid and arrested cells with complex karyotypes (obtained as described in Figure 6B). Graph shows the cytokine fold change in arrested cells with complex karyotypes normalized to euploid cells (mean ± SEM).

(C) Early passage wild-type and *BUB1B*$^{H/H}$ mouse embryonic fibroblasts were cultured and CCL2 levels were determined in culture supernatants (mean ± SD).

(D–G) MICA/B (D), CD155/PVR (E), and ULBP2 (F) cell surface levels in euploid cells and aneuploid arrested cells (obtained as described in Figure 6B). Euploid cells treated with doxorubicin (100 ng/mL, 48 hr) were used as a positive control for CD155/PVR and ULBP2 expression. Graphs show fluorescence intensity of cells of similar size (for gating see Figure S7). Immunoglobulin G_{2A} (IgG_{2A}) isotype control was used for MICA/B, ULBP2, and ULBP1 staining in euploid cells (Figure S7B). IgG_1 isotype control was used for CD155/PVR and Nectin-2/CD112 in euploid cells (Figure S7A). Mean fluorescence intensities are listed in (G).

(H) Euploid and arrested cells with complex karyotypes were generated as described in Figure 6B and levels of the indicated protein determined by ELISA (mean ± SEM).

(I) Euploid and arrested cells with complex karyotypes were generated as described in Figure 6B. Cells were co-cultured with NK92 cells at a target/effector ratio of 1:10 and filmed every 10 min for 36 hr. Representative images from live imaging datasets are shown.

(J) Euploid and aneuploid arrested cells were generated as described in Figure 6B. Cells were seeded and allowed to attach to the plate for 12 hr, after which NK92 cells were introduced. At the indicated times, dead and NK92 cells were removed by gentle shake-off and the remaining cells counted, and are shown as a percentage of cells grown for the same time in the absence of NK92 cells (mean ± SD). ***$p < 0.0001$; *$p < 0.05$; NS, not significant (ANOVA plus Bonferroni's test).

(K) Euploid and arrested cells with complex karyotypes and NK92 cells were cultured as in (J) for 24 hr. For experiments with antibodies blocking NKG2D, NK92 cells were pre-incubated with 20 μg/mL anti-NKG2D antibody for 3 hr before co-culturing them with RPE-1 cells. Dead and NK92 cells were removed, and the remaining cells counted and normalized to cells grown under the same conditions but without co-culture (mean ± SEM). ***$p < 0.0001$; NS, not significant (ANOVA plus Bonferroni's test).

See also Figures S6 and S7; Movie S3.

cell imaging (see STAR Methods). NK92 cells did not interact with euploid cells, but effectively killed cells with complex karyotypes (Figures 7I and 7J; Movie S3). NK92-mediated killing of aneuploid cells was not immediate but started 6–12 hr after mixing of cells (Figure 7J and Movie S3). Despite the fact that NK92-mediated killing occurred only after a lag, the response was nevertheless NK92 cell specific. Aneuploid arrested cells did not die when cultured in the absence of NK92 cells (Figure S7H).

Further evidence supporting the conclusion that selective killing occurred stems from the observation that the interaction between NK cells and aneuploid arrested cells was at least partially dependent on the NK cell receptor NKG2D. Pre-incubation of NK cells with blocking antibodies against NKG2D decreased their ability to kill aneuploid arrested cells (Figure 7K). We conclude that cells with complex karyotypes elicit an innate immune response aimed at their removal.

DISCUSSION

By investigating the immediate consequences of aneuploidy on cells, we identified mechanisms that eliminate aneuploid cells. Chromosome mis-segregation leads to genomic instability and increased karyotype complexity (Blank et al., 2015; Meena et al., 2015; Ohashi et al., 2015; Passerini et al., 2016; Sheltzer et al., 2011; Zhu et al., 2012; and this study). Cells with complex aberrant karyotypes ultimately cease to divide, exhibit features of senescence, and produce pro-inflammatory signals that promote their clearance by the immune system. Together, these findings indicate that multiple mechanisms prevent the accumulation of aneuploid cells in tissues. A senescence program limits their proliferation and the innate immune system facilitates their clearance. The latter mechanism could very well represent a means whereby cancer cells, which are frequently highly aneuploid, are recognized and eliminated by the immune system.

Cells Cannot Count Their Chromosomes

It was previously reported that chromosome mis-segregation induced by interference with spindle function causes p53 activation (Thompson and Compton, 2010). This observation led to the interesting proposal that the cells somehow ''know'' how many chromosomes they have and that a chromosome number that deviates from the euploid karyotype triggers a p53 response. However, chromosome mis-segregation brought about by interfering with spindle function results in a mitotic delay, which when it exceeds 100 min causes p53 activation in the subsequent G_1 phase irrespective of whether or not chromosome mis-segregation occurred (Uetake and Sluder, 2010), and requires the DNA damage binding protein 53BP1 and the deubiquitinating enzyme USP28 (Lambrus and Holland, 2017). To examine the effects of chromosome mis-segregation on cell-cycle progression without this complication, we used methods to interfere with chromosome segregation that accelerated rather than delayed mitosis. Live cell imaging of cells induced to mis-segregate chromosomes in this manner showed that the vast majority of cells that mis-segregate chromosomes do not delay or arrest in G_1 following chromosome mis-segregation. p53 activation and a p53-dependent cell-cycle arrest do not occur in cells harboring constitutive aneuploidies either (Sheltzer et al., 2017; Tang et al., 2011), further supporting the idea that aneuploidy per se does not trigger a p53-dependent G_1 arrest.

While the vast majority of cells that mis-segregated chromosomes continued to proliferate, some cells (10%–15%, depending on the experimental setup) do arrest in G_1. Such cells harbor highly complex karyotypes and show signs of DNA damage. We propose that DNA damage accrued during chromosome mis-segregation is largely responsible for p53 activation and G_1 arrest in these cells. In agreement with this hypothesis is the observation that inactivation of DNA damage-responsive kinases or p53 greatly reduces the number of cells that arrest in G_1 following chromosome mis-segregation. We further note that a previous study utilizing cells harboring a mutant allele of the SAC target Cdc20 ($CDC20^{AAA}$) that is resistant to SAC inhibition found that p53 is activated by the DNA damage checkpoint kinase ATM in aneuploid cells (Li et al., 2010). Several sources of DNA damage likely contribute to p53 activation. Lagging chromosomes might become trapped in the cytokinetic furrow (Janssen et al., 2011), which could lead to DNA damage but perhaps not breakage of chromosomes (Houchmandzadeh et al., 1997; Maciejowski et al., 2015). Premature anaphase entry induced by SAC inactivation could lead to anaphase onset in the presence of incompletely replicated or decatenated DNA. DNA damage could also occur when chromosomes contained in micronuclei are exposed to cytoplasmic nucleases, due to ruptured nuclear envelopes (Crasta et al., 2012; Hatch et al., 2013; Janssen et al., 2011). Aneuploidy-associated stresses that include oxidative, metabolic, and proteotoxic stress also likely contribute to p53 activation (Kruiswijk et al., 2015), especially in cells with high levels of genomic imbalances such as is seen in aneuploid cells that arrest in G_1. We conclude that the aneuploid state per se does not lead to p53 activation and G_1 arrest, whereas events associated with chromosome mis-segregation such as DNA damage and aneuploidy-associated stresses do. Thus, p53 activation is a potential but not an obligatory outcome of chromosome mis-segregation.

Aneuploidy Causes Chromosome Instability

Previous analyses showed that human and yeast cells harboring many different constitutive aneuploidies exhibit DNA replication and repair defects (Blank et al., 2015; Ohashi et al., 2015; Passerini et al., 2016; Sheltzer et al., 2011; Zhu et al., 2012). Here, we show that this effect on DNA replication is immediate. Our studies in yeast and those of others in mammalian cells further point to changes in the levels of DNA replication factors as being responsible for these DNA replication defects. In yeast, specific chromosome gains cause specific DNA replication and repair defects, indicating that altered expression of specific genes located on the aneuploid chromosome is responsible for the observed defects (Sheltzer et al., 2011; Zhu et al., 2012). In mammalian cells, multiple DNA replication factors such as the single-strand DNA binding protein RPA and the lagging-strand DNA polymerase δ have been shown to be haploinsufficient (Murga et al., 2016; O'Driscoll, 2008). Furthermore, aneuploid cells downregulate the expression of DNA replication proteins, such as the MCM helicases (Passerini et al., 2016).

The aneuploidy-induced aberrant S phase precipitates further chromosome instability. DNA damage incurred during the abnormal S phase persists into mitosis, leading to chromosome mis-segregation and other mitotic abnormalities. We note that this finding could provide an explanation for the puzzling observation that cancers harbor highly abnormal karyotypes, yet mutations in genes encoding chromosome segregation factors are rare in the disease (Kops et al., 2005). Our data show that a single chromosome mis-segregation event can set in motion the evolution of complex karyotypes that are characteristic of solid tumors.

Aneuploidy Causes an Innate Immune Response

Previous studies showed that aneuploidy is a rare occurrence in tissues even when chromosome segregation is compromised (Pfau et al., 2016), raising the possibility that mechanisms exist to eliminate cells with highly aberrant karyotypes in vivo. Our findings indicate that this is indeed the case. Cells with complex karyotypes express higher levels of NKG2D ligands, such as MICA/B and ULBPs, and of the DNAM1 ligands CD112 and CD155. These cell-surface molecules mediate NK cell activation,

trigger NK-mediated clearance in vitro (Iannello et al., 2013; Krizhanovsky et al., 2008), and have been shown to mediate tumor cell recognition (Raulet and Guerra, 2009).

Several characteristics of aneuploid cells likely contribute to their recognition by NK cells. For example, aneuploid arrested cells experience DNA damage and produce an SASP gene expression signature, which were previously shown to elicit NK cell recognition and to play a crucial role in the removal of cancer cells in vivo (Raulet and Guerra, 2009). Upregulation of genes regulated by the cGAS/STING pathway could hint at the presence of DNA in the cytoplasm in aneuploid arrested cells (Lan et al., 2014). The aneuploid state per se might also trigger immune recognition. MEFs harboring specific trisomies exhibit a gene expression pattern very similar to that of aneuploid arrested cells, yet these cells do not experience significant DNA damage nor undergo cell-cycle arrest. Aneuploidy causes a number of stresses such as proteotoxic stress and oxidative stress (Santaguida and Amon, 2015a), which have previously been shown to induce MICA/B and DNAM1-ligand expression, respectively (Raulet and Guerra, 2009). Moreover, it is important to note that the proteome of aneuploid cells is fundamentally altered because changes in gene copy number generally lead to changes in protein levels (Santaguida and Amon, 2015a). Aneuploidy-induced changes in the cell-surface proteome could also elicit an immune response.

It has not escaped our attention that our study could shed light on how the immune system recognizes cancer cells. Neoantigens have been proposed to be a major source of cancer immunosurveillance (Schumacher and Schreiber, 2015). Our data raise the possibility that immune recognition of cancer cells is also mediated by their aneuploid state and the physiological changes associated with complex aberrant karyotypes. At some point during disease evolution, however, aneuploid cancer cells escape immune detection and, once this point has been reached, aneuploidy appears to correlate with immune evasion (Davoli et al., 2017). Understanding which aspect of tumorigenesis transforms aneuploidy from an immunogenic trait into an immune evasive property will be key to understanding cancer immune evasion.

STAR★METHODS

Detailed methods are provided in the online version of this paper and include the following:

- KEY RESOURCES TABLE
- CONTACT FOR REAGENT AND RESOURCE SHARING
- EXPERIMENTAL MODEL AND SUBJECT DETAILS
- METHOD DETAILS
  - Drug Treatments
  - Isolation of Cells that Stopped Dividing Following Chromosome Mis-segregation
  - Cell Imaging Methods
  - Video Microscopy
  - Protein Detection by Western Blots
  - RNAseq Data Processing and Analysis
  - DNA Combing
  - Karyotype Analysis
  - Cytokine Measurement
  - ELISA Measurement
  - FACS
  - NK-Mediated Cell Death Assay
  - RNAi
  - β-Galactosidase Staining
- QUANTIFICATION AND STATISTICAL ANALYSIS
- DATA AND SOFTWARE AVAILABILITY

SUPPLEMENTAL INFORMATION

Supplemental Information includes seven figures, three tables, and three movies and can be found with this article online at http://dx.doi.org/10.1016/j.devcel.2017.05.022.

AUTHOR CONTRIBUTIONS

Conceptualization, S.S. and A.A.; Investigation, S.S., A.R., D.R.I., O.M., L.Z., K.A.K., and Y.L.W.; Writing, S.S. and A.A.; Funding Acquisition and Supervision, N.R., A.D., and A.A. All authors discussed the results and commented on the manuscript.

ACKNOWLEDGMENTS

We thank members of the A.A. laboratory for discussions and reading of the manuscript and Charlie Whittaker of the Barbara K. Ostrom (1978) Bioinformatics and Computing Facility in the Swanson Biotechnology Center for help with the gene expression analysis. We are grateful to Marianna Trakala for help and suggestions with FACS analysis. Work in the A.A. laboratory is supported by grants from the NIH (CA206157 and GM118066) and the Kathy and Curt Marble Cancer Research Fund. A.A. is an investigator of the Howard Hughes Medical Institute, the Paul F. Glenn Center for Biology of Aging Research at MIT, and the Ludwig Center at MIT. S.S. was supported by the American Italian Cancer Foundation (AICF), by a Fellowship in Cancer Research from Marie Curie Actions and the Italian Association for Cancer Research (AIRC), and by a KI Quinquennial Cancer Research Fellowship. K.A.K. is supported by National Institute of General Medical Sciences training grant T32GM007753. Work in the N.R. laboratory was supported by grant GM98815 from NIGMS. Work by the A.D. group is supported by grant GM074215 from NIGMS and by the Ludwig Institute for Cancer Research. A.R. acknowledges support from UC San Diego's Cancer Cell Biology training grant (NIH-NCI-T32-CA067754). We thank Andy Shiau (Head, Ludwig Small Molecule Discovery Group) for providing inhibitors and for access to high-content imaging and tissue culture equipment.

Received: August 30, 2016
Revised: March 7, 2017
Accepted: May 23, 2017
Published: June 19, 2017

REFERENCES

Baker, D.J., Jeganathan, K.B., Cameron, J.D., Thompson, M., Juneja, S., Kopecka, A., Kumar, R., Jenkins, R.B., de Groen, P.C., Roche, P., and van Deursen, J.M. (2004). BubR1 insufficiency causes early onset of aging-associated phenotypes and infertility in mice. Nat. Genet. *36*, 744–749.

Bakhoum, S.F., Danilova, O.V., Kaur, P., Levy, N.B., and Compton, D.A. (2011). Chromosomal instability substantiates poor prognosis in patients with diffuse large B-cell lymphoma. Clin. Cancer Res. *17*, 7704–7711.

Beach, R.R., Ricci-Tam, C., Brennan, C.M., Moomau, C.A., Hsu, P.-H., Hua, B., Silberman, R.E., Springer, M., and Amon, A. (2017). Aneuploidy causes non-genetic individuality. Cell *169*, 229–242.e21.

Blank, H.M., Sheltzer, J.M., Meehl, C.M., and Amon, A. (2015). Mitotic entry in the presence of DNA damage is a widespread property of aneuploidy in yeast. Mol. Biol. Cell *26*, 1440–1451.

Brunner, K.T., Mauel, J., Cerottini, J.C., and Chapuis, B. (1968). Quantitative assay of the lytic action of immune lymphoid cells on 51-Cr-labelled allogeneic

target cells in vitro; inhibition by isoantibody and by drugs. Immunology *14*, 181–196.

Chen, G., Mulla, W.A., Kucharavy, A., Tsai, H.-J., Rubinstein, B., Conkright, J., McCroskey, S., Bradford, W.D., Weems, L., Haug, J.S., et al. (2015). Targeting the adaptability of heterogeneous aneuploids. Cell *160*, 771–784.

Chien, Y., Scuoppo, C., Wang, X., Fang, X., Balgley, B., Bolden, J.E., Premsrirut, P., Luo, W., Chicas, A., Lee, C.S., et al. (2011). Control of the senescence-associated secretory phenotype by NF-κB promotes senescence and enhances chemosensitivity. Genes Dev. *25*, 2125–2136.

Colombo, R., Caldarelli, M., Mennecozzi, M., Giorgini, M.L., Sola, F., Cappella, P., Perrera, C., Depaolini, S.R., Rusconi, L., Cucchi, U., et al. (2010). Targeting the mitotic checkpoint for cancer therapy with NMS-P715, an inhibitor of MPS1 kinase. Cancer Res. *70*, 10255–10264.

Crasta, K., Ganem, N.J., Dagher, R., Lantermann, A.B., Ivanova, E.V., Pan, Y., Nezi, L., Protopopov, A., Chowdhury, D., and Pellman, D. (2012). DNA breaks and chromosome pulverization from errors in mitosis. Nature *482*, 53–58.

Davoli, T., Xu, A.W., Mengwasser, K.E., Sack, L.M., Yoon, J.C., Park, P.J., and Elledge, S.J. (2013). Cumulative haploinsufficiency and triplosensitivity drive aneuploidy patterns and shape the cancer genome. Cell *155*, 948–962.

Davoli, T., Uno, H., Wooten, E.C., and Elledge, S.J. (2017). Tumor aneuploidy correlates with markers of immune evasion and with reduced response to immunotherapy. Science *355*, eaaf8399.

Dodgson, S.E., Kim, S., Costanzo, M., Baryshnikova, A., Morse, D.L., Kaiser, C.A., Boone, C., and Amon, A. (2016). Chromosome-specific and global effects of aneuploidy in saccharomyces cerevisiae. Genetics *202*, 1395–1409.

Freund, A., Orjalo, A.V., Desprez, P.Y., and Campisi, J. (2010). Inflammatory networks during cellular senescence: causes and consequences. Trends Mol. Med. *16*, 238–246.

Gordon, D.J., Resio, B., and Pellman, D. (2012). Causes and consequences of aneuploidy in cancer. Nat. Rev. Genet. *13*, 189–203.

Hassold, T., and Hunt, P. (2001). To err (meiotically) is human: the genesis of human aneuploidy. Nat. Rev. Genet. *2*, 280–291.

Hatch, E.M., Fischer, A.H., Deerinck, T.J., and Hetzer, M.W. (2013). Catastrophic nuclear envelope collapse in cancer cell micronuclei. Cell *154*, 47–60.

Heilig, C.E., Löffler, H., Mahlknecht, U., Janssen, J.W.G., Ho, A.D., Jauch, A., and Krämer, A. (2009). Chromosomal instability correlates with poor outcome in patients with myelodysplastic syndromes irrespectively of the cytogenetic risk group. J. Cell. Mol. Med. *14*, 895–902.

Hewitt, L., Tighe, A., Santaguida, S., White, A.M., Jones, C.D., Musacchio, A., Green, S., and Taylor, S.S. (2010). Sustained Mps1 activity is required in mitosis to recruit O-Mad2 to the Mad1-C-Mad2 core complex. J. Cell Biol. *190*, 25–34.

Hinchcliffe, E.H., Day, C.A., Karanjeet, K.B., Fadness, S., Langfald, A., Vaughan, K.T., and Dong, Z. (2016). Chromosome missegregation during anaphase triggers p53 cell cycle arrest through histone H3.3 Ser31 phosphorylation. Nat. Cell Biol. *18*, 668–675.

Hodgkin, J. (2005). Karyotype, ploidy, and gene dosage. WormBook, 1–9.

Holland, A.J., and Cleveland, D.W. (2009). Boveri revisited: chromosomal instability, aneuploidy and tumorigenesis. Nat. Rev. Mol. Cell Biol. *10*, 478–487.

Houchmandzadeh, B., Marko, J.F., Chatenay, D., and Libchaber, A. (1997). Elasticity and structure of eukaryote chromosomes studied by micromanipulation and micropipette aspiration. J. Cell Biol. *139*, 1–12.

Iannello, A., Thompson, T.W., Ardolino, M., Lowe, S.W., and Raulet, D.H. (2013). p53-dependent chemokine production by senescent tumor cells supports NKG2D-dependent tumor elimination by natural killer cells. J. Exp. Med. *210*, 2057–2069.

Iyer, D.R., and Rhind, N. (2016). Analysis of DNA replication in fission yeast by combing. Cold Spring Harb. Protoc. http://dx.doi.org/10.1101/pdb.prot092015.

Iyer, D.R., and Rhind, N. (2017). Replication fork slowing and stalling are distinct, checkpoint-independent consequences of replicating damaged DNA. bioRxiv. http://dx.doi.org/10.1101/122895.

Janssen, A., van der Burg, M., Szuhai, K., Kops, G.J.P.L., and Medema, R.H. (2011). Chromosome segregation errors as a cause of DNA damage and structural chromosome aberrations. Science *333*, 1895–1898.

Knouse, K.A., Wu, J., Whittaker, C.A., and Amon, A. (2014). Single cell sequencing reveals low levels of aneuploidy across mammalian tissues. Proc. Natl. Acad. Sci. USA *111*, 13409–13414.

Kops, G.J.P.L., Weaver, B.A.A., and Cleveland, D.W. (2005). On the road to cancer: aneuploidy and the mitotic checkpoint. Nat. Rev. Cancer *5*, 773–785.

Krizhanovsky, V., Yon, M., Dickins, R.A., Hearn, S., Simon, J., Miething, C., Yee, H., Zender, L., and Lowe, S.W. (2008). Senescence of activated stellate cells limits liver fibrosis. Cell *134*, 657–667.

Kruiswijk, F., Labuschagne, C.F., and Vousden, K.H. (2015). p53 in survival, death and metabolic health: a lifeguard with a licence to kill. Nat. Rev. Mol. Cell Biol. *16*, 393–405.

Kyriakis, J.M., and Avruch, J. (2001). Mammalian mitogen-activated protein kinase signal transduction pathways activated by stress and inflammation. Physiol. Rev. *81*, 807–869.

Lambrus, B.G., and Holland, A.J. (2017). A new mode of mitotic surveillance. Trends Cell Biol. *27*, 314–321.

Lan, Y.Y., Londoño, D., Bouley, R., Rooney, M.S., and Hacohen, N. (2014). Dnase2a deficiency uncovers lysosomal clearance of damaged nuclear DNA via autophagy. Cell Rep. *9*, 180–192.

Lee, A.J.X., Endesfelder, D., Rowan, A.J., Walther, A., Birkbak, N.J., Futreal, P.A., Downward, J., Szallasi, Z., Tomlinson, I.P.M., Howell, M., et al. (2011). Chromosomal instability confers intrinsic multidrug resistance. Cancer Res. *71*, 1858–1870.

Li, M., Fang, X., Baker, D.J., Guo, L., Gao, X., Wei, Z., Han, S., Van Deursen, J.M., and Zhang, P. (2010). The ATM-p53 pathway suppresses aneuploidy-induced tumorigenesis. Proc. Natl. Acad. Sci. USA *107*, 14188–14193.

Lindsley, D.L., Sandler, L., Baker, B.S., Carpenter, A.T., Denell, R.E., Hall, J.C., Jacobs, P.A., Miklos, G.L., Davis, B.K., Gethmann, R.C., et al. (1972). Segmental aneuploidy and the genetic gross structure of the *Drosophila* genome. Genetics *71*, 157–184.

Lorke, D.E. (1994). Developmental characteristics of trisomy 19 mice. Acta Anat. (Basel) *150*, 159–169.

López-García, C., Sansregret, L., Domingo, E., McGranahan, N., Hobor, S., Birkbak, N.J., Horswell, S., Grönroos, E., Favero, F., Rowan, A.J., et al. (2017). BCL9L dysfunction impairs caspase-2 expression permitting aneuploidy tolerance in colorectal cancer. Cancer Cell *31*, 79–93.

Maciejowski, J., Li, Y., Bosco, N., Campbell, P.J., and de Lange, T. (2015). Chromothripsis and kataegis induced by telomere crisis. Cell *163*, 1641–1654.

Mayer, T.U., Kapoor, T.M., Haggarty, S.J., King, R.W., Schreiber, S.L., and Mitchison, T.J. (1999). Small molecule inhibitor of mitotic spindle bipolarity identified in a phenotype-based screen. Science *286*, 971–974.

Meena, J.K., Cerutti, A., Beichler, C., Morita, Y., Bruhn, C., Kumar, M., Kraus, J.M., Speicher, M.R., Wang, Z.Q., Kestler, H.A., et al. (2015). Telomerase abrogates aneuploidy-induced telomere replication stress, senescence and cell depletion. EMBO J. *34*, 1371–1384.

Minocherhomji, S., Ying, S., Bjerregaard, V.A., Bursomanno, S., Aleliunaite, A., Wu, W., Mankouri, H.W., Shen, H., Liu, Y., and Hickson, I.D. (2015). Replication stress activates DNA repair synthesis in mitosis. Nature *528*, 286–290.

Murga, M., Lecona, E., Kamileri, I., Díaz, M., Lugli, N., Sotiriou, S.K., Anton, M.E., Méndez, J., Halazonetis, T.D., and Fernandez-Capetillo, O. (2016). POLD3 is haploinsufficient for DNA replication in mice. Mol. Cell *63*, 877–883.

Niwa, O., Tange, Y., and Kurabayashi, A. (2006). Growth arrest and chromosome instability in aneuploid yeast. Yeast *23*, 937–950.

O'Driscoll, M. (2008). Haploinsufficiency of DNA damage response genes and their potential influence in human genomic disorders. Curr. Genomics *9*, 137–146.

Ohashi, A., Ohori, M., Iwai, K., Nakayama, Y., Nambu, T., Morishita, D., Kawamoto, T., Miyamoto, M., Hirayama, T., Okaniwa, M., et al. (2015). Aneuploidy generates proteotoxic stress and DNA damage concurrently with p53-mediated post-mitotic apoptosis in SAC-impaired cells. Nat. Commun. *6*, 7668.

Oromendia, A.B., Dodgson, S.E., and Amon, A. (2012). Aneuploidy causes proteotoxic stress in yeast. Genes Dev. *26*, 2696–2708.

Passerini, V., Ozeri-Galai, E., de Pagter, M.S., Donnelly, N., Schmalbrock, S., Kloosterman, W.P., Kerem, B., and Storchova, Z. (2016). The presence of extra chromosomes leads to genomic instability. Nat. Commun. *7*, 10754.

Pfau, S.J., Silberman, R.E., Knouse, K.A., and Amon, A. (2016). Aneuploidy impairs hematopoietic stem cell fitness and is selected against in regenerating tissues in vivo. Genes Dev. *30*, 1395–1408.

Raulet, D.H., and Guerra, N. (2009). Oncogenic stress sensed by the immune system: role of natural killer cell receptors. Nat. Rev. Immunol. *9*, 568–580.

Roper, R.J., and Reeves, R.H. (2006). Understanding the basis for Down syndrome phenotypes. PLoS Genet. *2*, e50.

Rutledge, S.D., Douglas, T.A., Nicholson, J.M., Vila-Casadesús, M., Kantzler, C.L., Wangsa, D., Barroso-Vilares, M., Kale, S.D., Logarinho, E., and Cimini, D. (2016). Selective advantage of trisomic human cells cultured in non-standard conditions. Sci. Rep. *6*, 22828.

Sansregret, L., Patterson, J.O., Dewhurst, S., López-García, C., Koch, A., McGranahan, N., Chao, W.C.H., Barry, D.J., Rowan, A., Instrell, R., et al. (2017). APC/C dysfunction limits excessive cancer chromosomal instability. Cancer Discov. *7*, 218–233.

Santaguida, S., and Amon, A. (2015a). Short- and long-term effects of chromosome mis-segregation and aneuploidy. Nat. Rev. Mol. Cell Biol. *16*, 473–485.

Santaguida, S., and Amon, A. (2015b). Aneuploidy triggers a TFEB-mediated lysosomal stress response. Autophagy *11*, 2383–2384.

Santaguida, S., Tighe, A., D'Alise, A.M., Taylor, S.S., and Musacchio, A. (2010). Dissecting the role of MPS1 in chromosome biorientation and the spindle checkpoint through the small molecule inhibitor reversine. J. Cell Biol. *190*, 73–87.

Santaguida, S., Vasile, E., White, E., and Amon, A. (2015). Aneuploidy-induced cellular stresses limit autophagic degradation. Genes Dev. *29*, 2010–2021.

Schneider, W.M., Chevillotte, M.D., and Rice, C.M. (2014). Interferon-stimulated genes: a complex web of host defenses. Annu. Rev. Immunol. *32*, 513–545.

Schumacher, T.N., and Schreiber, R.D. (2015). Neoantigens in cancer immunotherapy. Science *348*, 69–74.

Sheltzer, J.M., Blank, H.M., Pfau, S.J., Tange, Y., George, B.M., Humpton, T.J., Brito, I.L., Hiraoka, Y., Niwa, O., and Amon, A. (2011). Aneuploidy drives genomic instability in yeast. Science *333*, 1026–1030.

Sheltzer, J.M., Torres, E.M., Dunham, M.J., and Amon, A. (2012). Transcriptional consequences of aneuploidy. Proc. Natl. Acad. Sci. USA *109*, 12644–12649.

Sheltzer, J.M., Ko, J.H., Replogle, J.M., Habibe Burgos, N.C., Chung, E.S., Meehl, C.M., Sayles, N.M., Passerini, V., Storchova, Z., and Amon, A. (2017). Single-chromosome gains commonly function as tumor suppressors. Cancer Cell *31*, 240–255.

Stingele, S., Stoehr, G., Peplowska, K., Cox, J.U.R., Mann, M., and Storchova, Z. (2012). Global analysis of genome, transcriptome and proteome reveals the response to aneuploidy in human cells. Mol. Syst. Biol. *8*, 1–12.

Sullivan, K.D., Lewis, H.C., Hill, A.A., Pandey, A., Jackson, L.P., Cabral, J.M., Smith, K.P., Liggett, L.A., Gomez, E.B., Galbraith, M.D., et al. (2016). Trisomy 21 consistently activates the interferon response. Elife *5*, e16220.

Tang, Y.C., and Amon, A. (2013). Gene copy-number alterations: a cost-benefit analysis. Cell *152*, 394–405.

Tang, Y.C., Williams, B.R., Siegel, J.J., and Amon, A. (2011). Identification of aneuploidy-selective antiproliferation compounds. Cell *144*, 499–512.

Thompson, S.L., and Compton, D.A. (2010). Proliferation of aneuploid human cells is limited by a p53-dependent mechanism. J. Cell Biol. *188*, 369–381.

Torres, E.M., Sokolsky, T., Tucker, C.M., Chan, L.Y., Boselli, M., Dunham, M.J., and Amon, A. (2007). Effects of aneuploidy on cellular physiology and cell division in haploid yeast. Science *317*, 916–924.

Uetake, Y., and Sluder, G. (2010). Prolonged prometaphase blocks daughter cell proliferation despite normal completion of mitosis. Curr. Biol. *20*, 1666–1671.

Walther, A., Walther, A., Houlston, R., and Tomlinson, I. (2008). Association between chromosomal instability and prognosis in colorectal cancer: a meta-analysis. Gut *57*, 941–950.

Williams, B.R., Prabhu, V.R., Hunter, K.E., Glazier, C.M., Whittaker, C.A., Housman, D.E., and Amon, A. (2008). Aneuploidy affects proliferation and spontaneous immortalization in mammalian cells. Science *322*, 703–709.

Zhang, C.Z., Spektor, A., Cornils, H., Francis, J.M., Jackson, E.K., Liu, S., Meyerson, M., and Pellman, D. (2015). Chromothripsis from DNA damage in micronuclei. Nature *522*, 179–184.

Zhu, J., Pavelka, N., Bradford, W.D., Rancati, G., and Li, R. (2012). Karyotypic determinants of chromosome instability in aneuploid budding yeast. PLoS Genet. *8*, e1002719.

STAR★METHODS

KEY RESOURCES TABLE

REAGENT or RESOURCE	SOURCE	IDENTIFIER
Antibodies		
Anti-GAPDH	Santa Cruz	Cat# sc-365062; RRID: AB_10847862
Anti-γH2AX	Cell Signaling Technology	Cat# 9718; RRID: AB_2118009
Anti-53BP1	Novus	Cat# NB100-305; RRID: AB_10001695
Anti-PICH	Millipore	Cat# 04-1540; RRID: AB_10616795
Anti-BLM	Santa Cruz	Cat# sc-7790; RRID: AB_2243489
Anti-centromeric antibody	Antibodies Inc.	Cat# 15-234-0001
Anti-p53	Santa Cruz	Cat# sc-126; RRID: AB_628082
Anti-p21	Santa Cruz	Cat# sc-6246; RRID: AB_628073
Anti-p16	BD	Cat# 554079 RRID: AB_395229
Anti-Actin	Sigma-Aldrich	Cat# A2228; RRID: AB_476697
Anti-ULBP-2/5/6 PE-conjugated	R&D System	Cat# FAB1298P; RRID: AB_2214693
Anti-CD155/PVR PE-conjugated	R&D System	Cat# FAB25301P; RRID: AB_2269068
Anti-Nectin-2/CD112 PE-conjugated	R&D System	Cat# FAB2229P; RRID: AB_10890734
Anti-NKG2D/CD314	R&D System	Cat# MAB139; RRID: AB_2133263
Anti-ULBP-1 PE-conjugated	R&D System	Cat# FAB1380P
Anti-MIC A/B PE-conjugated	BD	Cat# 558352; RRID: AB_397077
Anti-IgG2A PE-conjugated	R&D System	Cat# IC003P; RRID: AB_357245
Anti-IgG1 PE-conjugated	R&D System	Cat# IC002P; RRID: AB_357242
Chemicals, Peptides, and Recombinant Proteins		
Fibronectin	Sigma Aldrich	F1141
Reversine	Sigma Aldrich or Cayman Chemical Company	R3904 (Sigma), 10004412 (Cayman)
AZ3146	Tocris	3994
Monastrol	Santa Cruz	sc-202710A
SB203580	Cell Signaling Technology	5633S
Nocodazole	Sigma Aldrich	M1404
Thymidine	Sigma Aldrich	T1895
Aphidicolin	Sigma Aldrich	A0781
RO-3306	Sigma Aldrich	SML0569
Chk2 inhibitor II hydrate	Sigma Aldrich	C3742
VE821	Cayman Chemical Company	17587
NMS-P715	EMD/Millipore	475949
Lipofectamine RNAiMAX	Life Technologies	13778
Critical Commercial Assays		
Click-iT EdU Alexa Fluor 647 or Alexa Fluor 488 Imaging Kit	Invitrogen	C10340, C10337
GenomePlex Single Cell Whole Genome Amplification Kit	Sigma Aldrich	WGA4
PathScan Inflammation Multi-Target Sandwich ELISA Kit	Cell Signaling Technology	7276
Senescence β-Galactosidase Staining Kit	Cell Signaling Technology	9860
Mouse cytokine array kit	R&D Systems	ARY006
Human cytokine array kit	R&D Systems	ARY005B
Deposited Data		
RNA-seq	This paper	https://www.ncbi.nlm.nih.gov/geo/; Accession number GEO: GSE83647

(*Continued on next page*)

Continued

REAGENT or RESOURCE	SOURCE	IDENTIFIER
Experimental Models: Cell Lines		
NK92-MI	ATCC	CRL-2408
RPE-1 hTERT	Gift of Iain Cheeseman (MIT)	NA
Bub1b$^{H/H}$ MEFs	(Baker et al., 2004)	NA
Oligonucleotides		
Mad2 siRNA	Life Technologies	4392420/s8391
Negative Control siRNA	Life Technologies	4390846
Software and Algorithms		
GraphPad Prism	N/A	http://www.graphpad.com
MATLAB	N/A	https://www.mathworks.com/products/matlab.html

CONTACT FOR REAGENT AND RESOURCE SHARING

Further information and requests for resources and reagents should be directed to and will be fulfilled by the Lead Contact, Angelika Amon (angelika@mit.edu).

EXPERIMENTAL MODEL AND SUBJECT DETAILS

RPE-1 hTERT cell lines and MEFs were cultured in DMEM (Invitrogen) supplemented with 10% FBS, 2 mM L-glutamine and 100 U/ml penicillin/streptomycin. Cells were grown at 37°C with 5% CO_2 in a humidified environment.

To generate an RPE-1 hTERT cell line co-expressing GFP-PCNA and H2B-RFP, cells were transduced with pBABE-Puro, a vector encoding human histone H2B C-terminally fused to mRFP1.3 (gift from Don Cleveland), and with an MGC collection human PCNA cDNA engineered to harbor an N-terminal eGFP fusion and cloned into pBABE-Hygro. A population of cells expressing both transgenes at moderate levels was selected by fluorescence activated cell sorting (FACS). This cell population was then cultured in DMEM/F12 (Invitrogen) supplemented with 10% FBS and 100U/ml penicillin/streptomycin and grown at 37°C with 5% CO_2 in a humidified environment.

NK92-MI cells were obtained from ATCC and cultured in Alpha Minimum Essential medium without ribonucleosides and deoxyribonucleosides but with 2 mM L-glutamine and 1.5 g/L sodium bicarbonate, 0.2 mM inositol, 0.1 mM 2-mercaptoethanol, 0.02 mM folic acid, horse serum to a final concentration of 12.5%, fetal bovine serum to a final concentration of 12.5%.

METHOD DETAILS

Drug Treatments

Reversine was obtained from Cayman Chemical or Sigma-Aldrich and used at a working concentration of 0.5 μM or 2μM; Monastrol (working concentration 100 μM) from Tocris; SB203580 (working concentration 10 μM) from CellSignalingTechnology; Thymidine (working concentration 5 mM), Aphidicolin (working concentration 400 nM), RO-3306 (working concentration 7.5 μM), Chk2 inhibitor II hydrate (working concentration 10 μM), VE821 (working concentration 1 μM) and Nocodazole (working concentration 330 nM) were obtained from Sigma-Aldrich. NMS-P715 (working concentration 1 μM) was obtained from EMD/Millipore.

Isolation of Cells that Stopped Dividing Following Chromosome Mis-segregation

To enrich for cells that ceased to divide following chromosome mis-segregation, RPE-1 cells were synchronized at the G_1/S phase transition by thymidine treatment. Six hours after release from the G_1/S phase block, cells were treated with vehicle or 0.5 μM reversine for 12 hours. After wash-out of the drug, cells were placed into fresh medium and either harvested 66 hours later (euploid and aneuploid cycling cells) or exposed to nocodazole. 12 hours later, mitotic cells were removed by shake-off and the remaining cells were placed again into fresh medium containing nocodazole. Because the percentage of dividing cells was very low after the fourth shake-off (see Figure 6B), we performed four nocodazole treatment/shake-offs in all experiments shown.

Cell Imaging Methods

For fluorescence imaging RPE-1 cells were plated at about 30% of confluence onto coverslips coated with 10 μg/ml Fibronectin (Sigma-Aldrich). Cells were fixed with 4% paraformaldehyde (in PBS) for 15 minutes at room temperature, then treated with 4% BSA-PBS and incubated with the appropriate antibodies diluted in BSA-PBS. The following antibodies were used for immunofluorescence: anti γH2AX (Cell Signaling Technology #9718), anti 53BP1 (Novus #NB100-305), anti PICH (Millipore #04-1540), anti BLM (Santa Cruz #sc-7790), anti-centromeric antibody (Antibodies Inc. #15-234-0001). Alexa 488- and Alexa 546-labeled secondary

antibodies were from Invitrogen. DyLight649-conjugated secondary antibody was purchased from Jackson ImmunoResearch Laboratories. DNA was stained with Hoechst. The coverslips were mounted using ProLong Gold Antifade reagent (Life Technologies).

EdU incorporation into DNA was visualized using the Click-iT EdU Alexa Fluor 647 or Alexa Fluor 488 Imaging Kit (Invitrogen) following the manufacturer's instructions. EdU-positive nuclei were scored by: (i) applying a global intensity threshold (manually adjusted to detect nuclei by Hoechst staining and EdU-positive cells at an intensity value of about 1000); (2) applying the Separate Touching Objects tool in Volocity; (3) excluding touching nuclei with a separation guide of 7 μm; and (4) rejecting nuclei with an area of less than 30 μm^2. The method was validated manually and found to give accurate cell counts.

Cells were imaged at 25°C on a Zeiss Axio Observer.Z1 inverted microscope (Zeiss. Thornwood, NY) with an ORCA-ER C4742-80 CCD camera (Hamamatsu Corporation. Middlesex, NJ) and an X-Cite Series 120 arc lamp (Life Sciences & Industrial Division. Ontario, Canada) or on a DeltaVision Elite imaging system (Applied Precision) and microscope (model IX-71; Olympus) controlled by SoftWoRx software (Applied Precision) and a 60× objective lens with a CoolSNAP HQ2 camera (Photometrics). Images were acquired as z-sections at 0.3 μm (DeltaVision) and converted into maximal intensity projections using SoftWoRx (Applied Precision) software. Deconvolution was performed using a constrained-iterative algorithm in SoftWoRx.

Quantification of fluorescence intensity as well as quantification of 53BP1 and γH2AX foci was conducted using Volocity (Perkin Elmer) and Python 2.7. γH2AX-positive foci within a cell were determined by analyzing the number of objects within each cell containing fluorescent accumulations of Hoechst and γH2AX greater than 0.2 μm^2 as measured by Volocity. Foci were scored by: (1) applying the Volocity "find spots" option; (2) filtering the population by applying a pixel intensity threshold of 1500; (3) using the compartmentalize tool in Volocity to analyze only previously identified nuclei; and (4) applying a 0.2 μm^2 size filter to remove speckles and noise. This protocol was validated manually and found to reliably detect foci. Images were imported into Photoshop CS5.1 (Adobe Systems, Inc.), and levels were adjusted.

For FISH analyses, RPE-1 cells were plated on 24x60mm coverslips, treated with DMSO or 1μM NMS-P715 for 24 hrs and then fixed and stained with Hoechst and FISH probes (Cytocell Aquarius Satellite Enumeration probe LPE-011G, Cytocell Aquarius Satellite Enumeration probe LPE-006R). Nuclei were imaged on a Deltavision microscope with a 40x objective and number of foci/nucleus were counted.

Video Microscopy

Live cell imaging was performed either using an inverted microscope (IX70; Nikon) with a magnification objective of 10x or using a Yokagawa CQ1 spinning disk confocal (40x objective, reversine-treated cells) or Yokogawa CV1000 (20x objective, monastrol-treated cells). All microscopes were equipped with an incubation chamber maintained at 37°C in an atmosphere of 5% CO_2. For experiments with NK92 cells, euploid and aneuploid arrested cells were co-cultured in the presence of NK92 cells at a target:effector ratio of 1:10 right before the beginning of filming.

For experiments described in Figure S1, unsynchronized RPE-1 hTERT GFP-PCNA H2B-RFP cells were plated on Greiner SCREENSTAR 96-well plates (#655866), incubated overnight, and then treated with DMSO or 100 μM monastrol and immediately filmed for 6 hrs using a Yokagawa CV1000 microscope with a 20x objective. After 6 hours plates were removed, cells were washed twice with complete medium, and returned to the microscope for an additional 50 hrs of filming. Because cells were unsynchronized, mother cells entered mitosis throughout monastrol treatment and thereby experienced variable mitotic delays. After drug washout, the mother cells exited mitosis and the cell cycle progression of their daughter cells was tracked. Images were acquired every 10 min for the first 8 hrs to capture mother cell mitotic timing and mis-segregation events, and then every 20 min to capture daughter cell cycle progression.

To quantify daughter cell S phase timing after chromosome mis-segregation in the mother cell, unsynchronized RPE1 hTERT GFP-PCNA H2B-RFP cells were plated on Greiner SCREENSTAR 96-well plates (#655866), incubated overnight, and then treated with DMSO, 0.5 μM, or 2 μM reversine. Cells were immediately filmed on a Yokagawa CQ1 with a 40x objective. Images were acquired every 5 minutes for 5 hrs and then every 20 min for a total of 48 hrs. Reversine was not washed out for the duration of the experiment. Because cells were unsynchronized, we determined the time from PCNA focus appearance to disappearance for two types of cells. The first type (G_1) were cells that progressed through mitosis before drug treatment and hence were exposed to reversine only during G_1 and S phase. The second type (G2) were the daughters of mother cells that progressed through mitosis in the presence of reversine and had mis-segregated their chromosomes.

To track daughter cell cycle fate after mother cells had mis-segregated chromosomes, RPE-1 hTERT GFP-PCNA H2B-RFP cells were plated on 96-well cycloolifin plates overnight, treated with DMSO or 1 μM NMS-P715 and immediately filmed on a Yokagawa CV1000 microscope using a 20x objective. Images were acquired every 10 min for 8 hrs to capture mother cell mitosis and then every 15 min for 2 days to track daughter cell fate.

Protein Detection by Western Blots

For protein analyses cells were lysed in lysis buffer (50 mM Tris-HCl, pH8.0, 150 mM NaCl, 0.5 % Sodium deoxycholate, 0.1% SDS, 1% NP-40, protease inhibitor cocktail (Roche) and phosphatase inhibitor cocktail (Roche)) and resolved on 15% SDS PAGE gels. The following primary antibodies were used: anti-actin (Sigma-Aldrich #A2228, 1:10,000), anti-p53 (Santa Cruz #sc-126, 1:200), anti-p21 (Santa Cruz #sc-6246, 1:200), anti-p16 (BD #554079, 1:200), anti γH2AX (Cell Signaling Technology #9718, 1:500), anti-GAPDH (Santa Cruz #sc-365062).

RNAseq Data Processing and Analysis

RNAseq analyses were conducted on euploid, and aneuploid cells that proliferate or that had ceased to divide. Total RNA was isolated using the RNeasy Mini Kit (QIAGEN). Quality control of single end reads was performed by aligning reads to the human genome (hg19) with tophat 2.0.9. Alignment rates to various genomic features were counted and summarized using bedtools 2.17.0 and a series of custom scripts. The QC results are all within acceptable ranges.

To quantify gene expression, RNAseq data were aligned and summarized using bowtie version 1.0.1, rsem version 1.2.15, samtools/0.1.19 and a UCSC known genes annotation file from the hg19 assembly. Differential expression analysis was performed with R version 3.2.2 and DESeq_1.20.0. Raw data for the trisomic MEF experiment (GSE12501) and senescence experiment (GSE11954) were downloaded from GEO and reprocessed using R version 3.2.2 with bioconductor packages affy_1.48.0, affyPLM_1.46.0 and gcRMA_2.42.0. For the senescence experiment, markers of growth and senescence were identified by differential expression analysis using limma_3.26.3 with statistical cut-offs of log2 fold change > 1 and adjusted p-value < 0.05.

Gene Set Enrichment Analysis was run with Java application version 2.2.2 obtained from the Broad Institute and custom gene sets (sting_sasp.gmx, grVsen_degs.gmx) or canonical pathway gene sets (c2cp) available at MsigDB (http://software.broadinstitute.org/gsea/msigdb/index.jsp). Genes with low average expression and variance across all samples (expression < 0.5, variance < 0.02) were excluded from the GCT file.

A group of histone genes shows some degree of differential expression in our experiment and these genes are found in many different c2cp gene sets such as REACTOME_RNA_POL_I_TRANSCRIPTION and REACTOME_MEIOTIC_RECOMBINATION. These gene sets show enrichment in our arrested cells with complex karyotypes. Because our experiment depends on polyA tail purification of mRNAs for sequencing and given the controversy surrounding the polyA status of histone mRNAs, we have excluded the gene sets dominated by histone genes from our GSEA summary in order to highlight other biological processes.

DNA Combing

RPE-1 cells were treated with 0.5 μM reversine or vehicle control for 24 hours. The cells were then washed and arrested in late G_1 by treatment with Mimosine for 24 hours. Mimosine was removed and cells were placed into fresh medium. Three hours later cells were pulsed at 37°C with 25 μM IdU for 60minutes and chased with 200 μM CldU for 60 minutes. After labeling, cells were harvested and washed twice with PBS. Cells were re-suspended in 50 μl of PBS to a final concentration of $0.5x10^6$ cells/ml. Cells were incubated at 42°C for 2-3 minutes and mixed with equal volume of 1.5 % low melting agarose (made in PBS and pre-warmed to 42°C) and cast into plug molds and allowed to set at 4°C for half an hour. The plugs were digested with Proteinase K for a total of 60 hours at 50°C with solution changes every 12 hours. The plugs were washed with TE and the combed fibers were stained as previously described (Iyer and Rhind, 2016). Fibers were visualized using a Zeiss Axioskop 2 Plus epifluorescence microscope with a 100x Plan-NEOFLUAR oil objective and imaged using a SPOT monochrome cooled-CCD camera. Fibers were measured using ImageJ. Pixels were converted to kb using λ DNA as a standard. Analysis of the data was automated using custom-made MATLAB scripts.

For fork stall rate estimation, two unidirectional forks moving in the same direction on a fiber (green-red-unlabeled-green-red or red-green-unlabeled-red-green) were inferred to contain a stalled fork in between them. Specifically, stalled forks were recognized by red-unlabeled-green (RUG) or green-unlabeled-red (GUR) patterns. The frequency of such patterns in the dataset was used to identify the apparent stall rate. In addition, two forks moving away from each other on a fiber (a RGUGR pattern) can be interpreted as forks elongating from a single origin in the middle or two origins whose forks on the inner side have both stalled. To estimate the stall rate across the entire dataset, the probability of forks stalling was estimated from the unambiguous stall events and extrapolated to ambiguous events to determine the net stall rate (Iyer and Rhind, 2017).

Karyotype Analysis

Karyotype determination by single cell sequencing was performed as previously described (Knouse et al., 2014). Briefly, single cells were isolated by microaspiration, and genomic DNA was amplified using the GenomePlex Single Cell Whole Genome Amplification Kit (Sigma). Amplified DNA was purified, barcoded, pooled, and sequenced on an Illumina HiSeq2000. Sequencing reads were aligned using BWA (0.6.1). HMMcopy (0.1.1) was used to estimate gene copy number in 500-kb bins. Cells with high variability in copy number across bins were excluded from the analysis.

Karyotype analysis by G-banding was performed by Cell Line Genetics (Madison, WI).

Cytokine Measurement

Euploid and arrested cells with complex karyotypes were isolated and placed into fresh medium for 36 hours. Then, medium was harvested and cell number determined using a Cellometer AutoT4 (Nexcelom). Levels of secreted cytokines were determined using the human cytokine array kit (R&D Systems) following the manufacturer's instructions and normalized to total number of cells.

ELISA Measurement

Euploid and arrested cells with complex karyotypes were isolated and the levels of NF-κB p65, phospho- NF-κB p65 (Ser536), phospho-SAPK/JNK (Thr183/Tyr185), phospho-p38 MAPK (Thr180/Tyr182), phospho-Stat3 (Tyr705) and phospho-IκB-α (Ser32) were measured by a solid phase sandwich enzyme-linked immunosorbent assay (PathScan Inflammation Multi-Target Sandwich ELISA Kit, Cell Signaling Technology) following the manufacturer's instructions.

FACS

Euploid and arrested cells with complex karyotypes were generated as described above and the levels of MICA/B, CD155/PVR, CD112, ULBP1 and ULBP2 were measured by flow cytometry and analyzed using FlowJo software. Forward (FSC-A) scatter was used to determine the cell size distribution of the cell population.

NK-Mediated Cell Death Assay

^{51}Chromium release assays are traditionally used to determine the cytotoxicity of immune cells (Brunner et al., 1968). Because of concerns over spillage during the repeated nocodazole shake-offs necessary to generate aneuploid arrested cell populations, we did not use this assay. Instead we followed cell killing by life-cell microscopy. In this assay, euploid and aneuploid arrested cells were generated as described above and plated into a 12 well plate at 10^4 cells/well. 12 hours later, cells were placed in NK92 growth medium for 24 hours and then co-cultured in the presence of NK92 cells at a target:effector ratio of 1:10 for 24 hours. For antibody-blocking experiments, NK92 cells were pre-incubated with 20 μg/ml anti-NKG2D antibody (R&D systems) for three hours. Dead cells, together with NK92 cells, were gently removed. Adherent cells were counted using a Cellometer AutoT4 (Nexcelom) and normalized to cells grown under the same condition but in the absence of NK92 cells.

We note that the kinetics of NK92 cell mediated killing of aneuploid arrested cells is slower than what is usually seen with the ^{51}Chromium release assay (Brunner et al., 1968). This difference could be biological, that is NK92 cells take longer to become activated by aneuploid arrested cells than by other target cells. We favor the idea that differences in assay sensitivity are responsible for the slow NK92 cell response that we observe. To detect release of ^{51}Chromium from cells membrane perforation has to occur. In contrast, life cell imaging based assessment of cell death requires the complete lysis of cells, which is likely to take longer than membrane perforation.

RNAi

For RNAi experiments, RPE-1 cells were plated at about 25-30% of confluence 12 hours before transfection. Negative control siRNA (with sequence that do not target any gene product) or oligos targeting Mad2 were purchased from Life Technologies (catalogue number 4390846 and 4392420/s8391, respectively) and transfected with Lipofectamine RNAiMAX (Life Technologies) at final concentration of 10 nM following the manufacturer's instruction.

β-Galactosidase Staining

Euploid and arrested cells with complex karyotypes were plated into a 6 well plate at 10^6 cells/well, allowed to attach overnight, and then stained using the Senescence β-Galactosidase Staining Kit (Cell Signaling Technology) following the manufacturer's instructions.

QUANTIFICATION AND STATISTICAL ANALYSIS

Statistical analysis was performed using GraphPad Prism software. Details of the statistical tests employed are reported in figure legends. Error bars represent SEM unless otherwise indicated. All experiments were performed in two or more replicates and at least 50 cells/condition/replicate were analyzed.

DATA AND SOFTWARE AVAILABILITY

The RNA-seq data sets generated for this study can be accessed at Gene Expression Omnibus (GEO) database with the accession number GEO: GSE83647.